A COMPRESSIBLE RECONFIGURABLE FREQUENCY SELECTIVE SURFACE

A Thesis

by

SHULI LI

Submitted to the Office of Graduate and Professional Studies of
Texas A&M University
in partial fulfillment of the requirements for the degree of

MASTER OF SCIENCE

Chair of Committee,	Gregory Huff
Committee Members,	Kai Chang
	Arum Han
	Yuefeng Sun
Head of Department,	Miroslav M. Begovic

May 2015

Major Subject: Electrical Engineering

ABSTRACT

Frequency selective surfaces (FSSs) are periodic structures which perform a spatial filtering operation, such as band-pass, band-stop, etc. in application of multiband reflector antennas, radomes, absorbers and so on. The filtering is normally achieved by periodic arrangement of metallic shapes or slots on a dielectric slab. The responses of the FSS are impacted by the unit cell structure, type of the element, material properties and arrangement of the array. The interest in frequency agile and wideband systems has led to an expanding design space to include reconfigurable FSSs. Reconfigurable FSSs have the advantages of wider range of operating frequencies, compensation for fabrication errors by tuning mechanically. The reconfiguration could be achieved by solid-state devices (varactors, PIN diodes), usage of semiconductors, changing the substrates' characteristics or the dimensions of the elements. Tunable FSS are in practical need for applications such as tunable radomes and adaptive screening of unwanted wireless transmissions. For a continuous tuning over the frequency range, fluidic tuning and mechanical reconfigurable FSSs claim to deliver the most dramatic continuous parameter variations.

In this work, a 3-D mechanically tunable FSS has been presented with a band-stop characteristic. The 3-D FSSs has displayed greater flexibility and controllability compared to conventional 2D FSSs. They have the ability of setting the resonant frequency and continuous tuning the operational filter states with a change in length or height of the resonator, offering the tuning and switching functionality from the same

structure without the use of additional electrical components. In this design, the reconfiguration is achieved by compressing the FSS structure, varying the height and the element shapes. Simulations and measurements of a FSS prototype manufactured by 3-D printer, some metallic and dielectric components are provided to demonstrate the tuning capability in S-band. A 490 MHz tuning range could be achieved by this design, while adding some dielectric material inside, a wider tuning range of 600 MHz could be reached. The measurement results show a good match with the design by HFSS.

ACKNOWLEDGEMENTS

I would like to thank my committee chair, Dr. Huff, for his guidance and support throughout the course of this research. Thank you to my other committee members, Dr. Chang, Dr. Han and Dr. Sun for their participation on my committee.

Thanks to Michael Kelly for his help and suggestions in the FSS measurement, Thanks to David Grayson for his help to mill out the Duroid disks. Thanks also go to my friends and colleagues and the department faculty and staff for making my time at Texas A&M University a great experience. I also want to extend my gratitude to the U.S. National Science Foundation for their support.

Finally, thanks to my mother and father for their encouragement and love.

NOMENCLATURE

FSS	Frequency Selective Surface
RF	Radio Frequency
MEMS	Microelectromechanical System
3-D	Three Dimensional
HFSS	High Frequency Structural Simulator
TE	Transverse Electric
TM	Transverse Magnetic
dB	Decibels
GHz	Gigahertz
S_{12}	Transmission Coefficient
EM	Electromagnetic
PLA	Polylactic Acid
DUT	Device under Test
TRL	Through, Reflect, Line
SOLT	Short, Open, Load, Through
THRU	Through

TABLE OF CONTENTS

Page

LIST OF FIGURES

LIST OF TABLES

CHAPTER I

INTRODUCTION AND BIO-INSPIRED MOTIVATION

Frequency selective surfaces (FSSs) are periodic structures which perform a filter operation. Depending on their physical construction, material and geometry, they could provide different filter responses (i.e. band-pass, band-stop, etc.). Possible applications include multiband reflector antennas, radomes, absorbers, artificial electromagnetic bandgap materials and optical filters [1, 2]. One limitation of the FSS in practical application turns out to be the relative large size since there has to be enough periodic unit cells to create desired performance, so that it is more applicable in aerospace and military applications than consumer products.

The interest in frequency agile and wideband systems such as multiband communication systems, flexible transceivers has led to an expanding design space to include reconfigurable FSSs. Reconfigurable FSSs have the advantages of wider range of operating frequencies, compensation for fabrication errors by tuning mechanically. The reconfiguration could be achieved by several different methods such as integration of nonlinear devices (varactors, PIN diodes), changing the substrates' characteristics or changing the dimensions of the elements [3], using a semiconductor as a substrate and illuminating the substrate to change the conductivity of substrate [4]. Tunable FSS could be able to replace complex sets of FSSs consisting of numerous fixed FSSs and switches, achieving a low cost, low loss and more flexible RF front end.

This work presents a reconfigurable FSS which achieves tuning through a compressible structure. The idea comes from an interesting biological phenomenon. Some animals have the ability to change their skin color and patterns to help adapt to the environments, for example: cephalopods (octopus, cuttlefish and etc.), they are able to use this feature to help them adapt to diverse marine environments. They are also using this feature to signal and communicate with their own species and others. This biological skin adaptive coloration can be explained by Figure 1.1 [5].

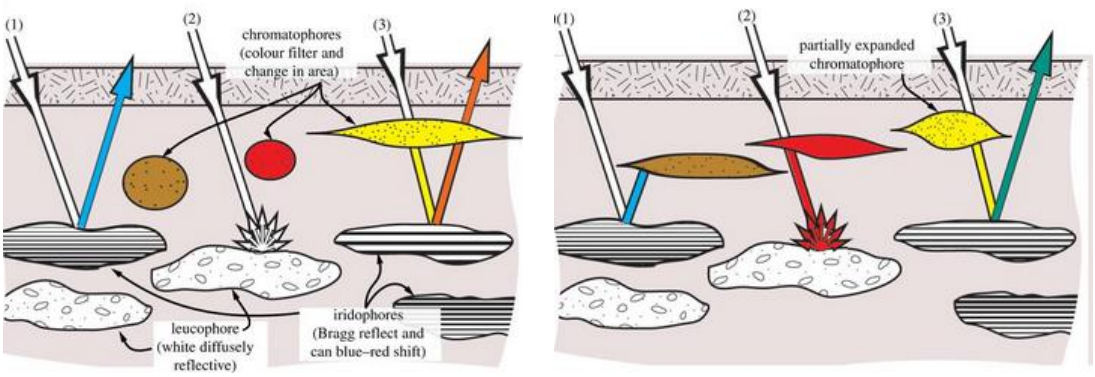

(a) (b)

Figure 1.1 Diagram of cephalopod skin detailing the three main skin structures (chromatophores, iridophores and leucophores)

There are three main skin structures: chromatophores, iridophores and leucophores. Chromatophores are in charge of the changing the coloration of the skin, named color filters. The ray trace 1 in Figure 1.1 (a) shows a ray of white light incident on an iridophore cell. Owing to constructive interference, the reflected light is blue (shorter wavelength), given by the periodic spacing for the iridophore. The ray trace 1 in Figure 1.1 (b) shows the expanded brown chromatophore absorbing most of the reflected

blue light. The ray trace 2 in Figure 1.1 (a) shows diffusely reflected white light from a leucophore, which in Figure 1.1 (b) is colored red by the expanded red chromatophore. The ray trace 3 in Figure 1.1 (a) depicts incident light filtered by a yellow chromatophore, and then reflected from an iridophore with a plate spacing shifted closer to the red spectrum such that the reflected light is orange. The ray trace 3 in Figure 1.1 (b) shows the same yellow-filtered light appearing greenish as the iridophore plate spacing decreased (wavelength shift towards cyan/blue). These color filters are able to filter out different colored light by changing the shape and spacing between those structures. An electromagnetic application has been inspired by this structure, shown in Figure 1.2.

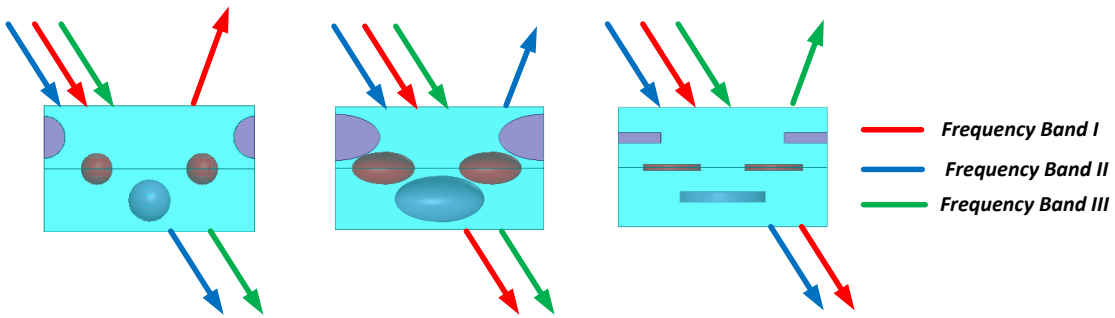

Figure 1.2 Electromagnetic application inspired by the cephalopod

In this work, a compressive reconfigurable FSS has been designed with a structure similar to chromatophores in Figure 1.1. There are several balls in the FSS in control of the electromagnetic waves operating in different frequency ranges. For example, in Figure 1.2, when the FSS is in the ball state, the frequency band I is reflected back while frequency band II and III has been transmitted. By compressing the

FSS, the shape and spacing of the balls will change, leads to a change in the resonant frequency and bandwidth, achieving a reconfigurable capability, like in Figure 1.2 when they the FSS is compressed into ellipsoid and disk state, the response of the FSS has been changed. Different frequency bands are reflected and transmitted.

In this thesis, some background knowledge related to this work will be explained in Chapter II. In Chapter III, conceptual circuit modeling will be provided in the analysis of the tunable FSS. Full-wave simulations will be used to predict the physical FSS performance with the estimated material properties, due to fabrication difficulties, a second iteration of the design has been performed with an applicable fabrication method. Chapter IV discusses about a prototype fabricated by the 3-D printer and measured by a network analyzer to demonstrate the conceptual model. A discrepancy between simulated and fabricated model leads to an analysis in the material properties and fabrication issues in Chapter V. The FSS was re-simulated with the correct parameters. Finally, a conclusion and the design summary are presented in Chapter VI.

CHAPTER II

BACKGROUND

FSS Overview

FSSs are periodic structures which perform a filter operation. Depending on their physical construction, material and geometry, they could provide different filter responses (i.e. band-pass, band-stop, etc.). Fundamentally, the FSS can be excited by an incident plane wave $\overrightarrow{E^i}$, as shown in Figure 2.1 [1]. The incident plane wave will be partly transmitted in the forward direction: $\overrightarrow{E^t}$ and partly reflected in the specular direction as $\overrightarrow{E^r}$.

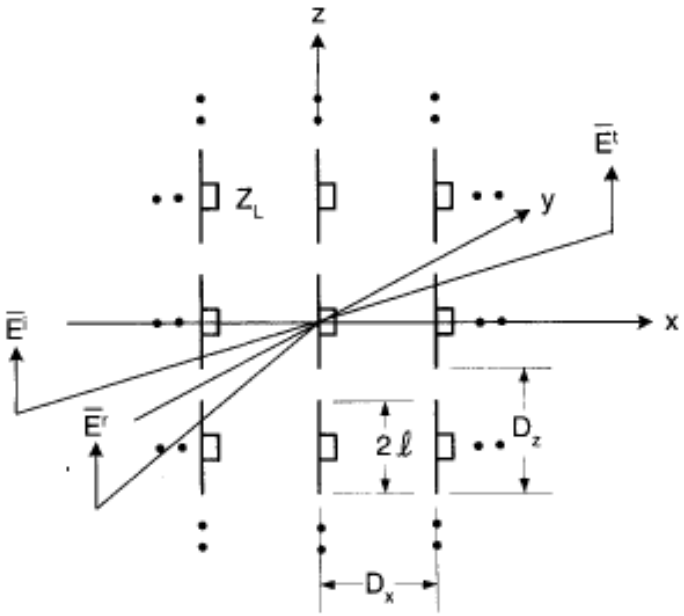

Figure 2.1 FSS excited by plane wave

It is commonly to fine the transmission coefficient as:

$$\tau = \frac{E^t}{E^i} \tag{2.1}$$

Similarly the reflection coefficient could be defined as:

$$\Gamma = \frac{E^r}{E^i} \tag{2.2}$$

Where the E^r, E^t and E^i in general are reference to the plane of the array. For a lossless network, conservation of energy simply requires for the reflection and transmission coefficient, so that:

$$\Gamma^2 + \tau^2 = 1 \tag{2.3}$$

From Equation (1.3) it is obvious to see with a high value of transmission coefficient, the reflection coefficient drops automatically.

In general, the FSS structure can be categorized into two major groups: patch-type element and aperture-type element. As an overview of the FSS structure, two complementary planar arrays are commonly considered: dipole arrays and slot arrays, shown in Figure 2.2 and they have band-stop and band-pass response respectively.

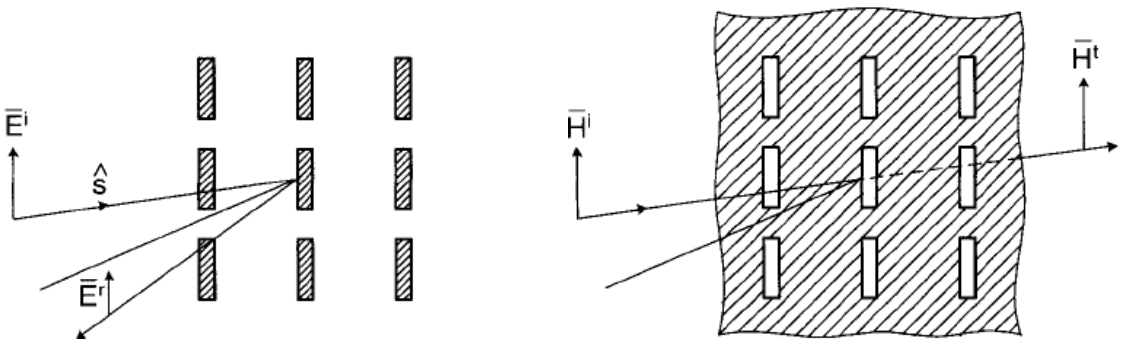

(a) (b)

Figure 2.2 Simple examples of complementary arrays: (a) dipole array (b) slot array

Over the years, a lot of FSS elements were introduced for either a band-stop or band-pass FSS, the choice of a proper element is one of the most important things to consider. There are four common element types available for FSS designers of today: center connected type, loop type, plate type and combination type [1]. Several examples of the four types of elements are shown in Figure 2.3. Depending on the application requirements, different FSS designs can be chosen to fulfill the demands. For example, loop type elements have good angel stability characteristic so that they are widely used for broadband applications [6], while the solid plate type element has a limitation of large size, but is used in conjunction with a complementary FSS.

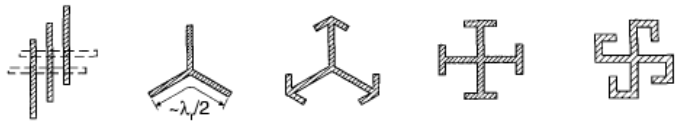

(a) Center connected or N poles

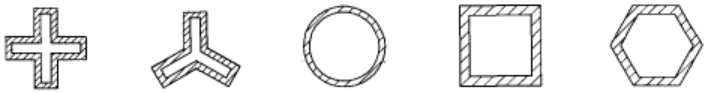

(b) Loop type

(c) Solid Interior or plate type

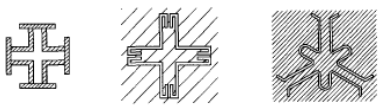

(d) Combination

Figure 2.3 Typical element types for FSS design

Reconfigurable RF/Microwave Devices

Since the past decades, the emerging needs for multi-band and multi-function specifications within the same design platform has stimulated the significant development of reconfigurable/ tunable devices and circuits in the field of RF and microwave wireless systems. There are typically two different methods of tuning components and methods. The first method is using tuning elements like PIN diodes and microelectromechanical system (MEMS) switches [7-8], and could have discrete tuning states. This method would not cover the entire tuning range. The second method is by using tunable elements such as varactor diodes, MEMS capacitors, or fluidic tuning systems capable of continuous reconfiguration for microwave and RF devices [9]. Some examples of fluidic tuning mechanism that has been incorporated in RF/microwave devices are: tunable dielectric resonator antenna [10], impedance transformer [11], reflect array element [12], and substrate integrated waveguide resonator [13].

The reconfigurable FSSs are in practical need for applications such as tunable radomes and adaptive screening of unwanted wireless transmissions [14]. The above methods mentioned for reconfigurable RF/microwave devices are applicable to reconfigurable FSSs. However, they also suffer from the same problem: the solid-state devices are nonlinear and cannot provide continuous tuning over the frequency range. Moreover, the huge demand of active elements will again increase cost, complexity and the potential for failure [15], [16]. Mechanical reconfigurable FSSs claim to deliver the most dramatic continuous parameter variations. It can be implemented by shifting one layer of double-layer FSS, hence altering the resonant frequency [17], the relative shift

between two layers changes the coupling capacitance between two layers. Another mechanical reconfiguration technique introduces pneumatically actuation in change of the unit cell geometry [18].

Recently, the innovative concept of three-dimensional (3-D) FSSs has displayed greater flexibility and controllability [19] compared to conventional 2D FSSs. They have the ability of setting the resonant frequency and continuous tuning the operational filter states with a change in length or height of the resonator, offering the tuning and switching functionality from the same structure without the use of additional electrical components. In this work, the compressible reconfigurable FSS is a mechanically tuned 3-D FSS, varying the height of the structure, the resonant frequency can be adjusted, while on the other hand changing he capacitance between layers.

Network Analysis

In this work, the analysis of the reconfigurable FSS is based on a two-port network as shown in Figure 2.4 and signal flow graph showing in Figure 2.5. a_i is identified with a wave entering port i, while b_i is identified with a wave reflected from port i. The useful voltage and current techniques for analyzing low-frequency cannot be directly applied to microwave circuits. The network analyzer commonly measures the reflection and transmission of the microwave network in terms of S parameters.

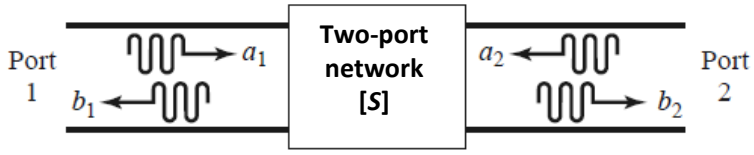

Figure 2.4 Two port network with incident and reflected waves

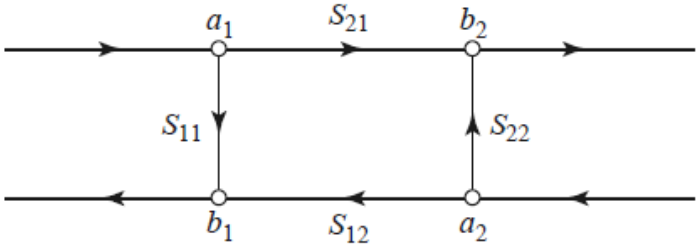

Figure 2.5 Two port network signal flow graph

The *S* parameters of a two-port network relate the incident and reflected wave from all ports, and can be measured directly from a network analyzer. The *S* parameters are defined in terms of the wave variables in Figure 2.4. S_{11}, S_{22} are the reflection coefficients seen looking into port 1 and port 2 respectively. S_{12} is the transmission coefficient from port 2 to port 1, and S_{21} is the transmission coefficient from port 1 to port 2, a_i=0 implies a perfectly impedance match at port *i*.

$$S_{11} = \left.\frac{b_1}{a_1}\right|_{a_2=0} \qquad S_{12} = \left.\frac{b_1}{a_2}\right|_{a_1=0} \tag{2.4}$$

$$S_{21} = \left.\frac{b_2}{a_1}\right|_{a_2=0} \qquad S_{22} = \left.\frac{b_2}{a_2}\right|_{a_1=0}$$

The *S* parameters can also be written as a set of linear equations in matrix noted as scattering matrix:

$$\begin{bmatrix} b_1 \\ b_2 \end{bmatrix} = \begin{bmatrix} S_{11} & S_{12} \\ S_{21} & S_{22} \end{bmatrix} \begin{bmatrix} a_1 \\ a_2 \end{bmatrix} \tag{2.5}$$

There are two special cases for the scattering matrix, for a reciprocal network it is symmetric, equation (2.6) and for a lossless network is unitary (2.7).

$$S_{ij} = S_{ji} \text{ for all } i, j \tag{2.6}$$

$$\sum_{k=1}^{N} S_{ki} S_{kj}^{*} = \delta_{ij} \tag{2.7}$$

Where $\delta_{ij} = 1$ if $i = j$ and $\delta_{ij} = 0$ if $i \neq j$.

The limits and physical interpretations of the S parameters are defined in Table 2.1.

Table 2.1 Limits and physical interpretations of two-port network *S* parameters

	S_{11}	S_{12}	S_{21}	S_{22}
0 dB	total reflection at port 1	total transmission from port 2 to 1	total transmission from port 1 to 2	total reflection at port 2
-∞ dB	total transmission through port 1	no transmission from port 2 to 1	no transmission from port 1 to 2	total transmission through port 2

CHAPTER III

ANALYSIS OF COMPRESSIBLE FREQUENCY SELECTIVE SURFACE

Two design iterations have been conducted in this work with similar structure and reconfiguration mechanism, the first design has some manufacturing difficulties thus a second design has been presented. Details of the design and some conceptual circuit analysis will be discussed in this chapter.

Design Iteration I

In this work, a compressible FSS with two substrate layers have been designed. Conducting balls of the same size are placed inside the two layers, one in the bottom layer and four quarter balls at the four corners of the top layer, illustrated in Figure 3.1. The dielectric balls are placed in the center of the FSS unit cell and are sandwiched by the two conducting balls, with half of the ball in the up substrate layer and the other half in the bottom layer shown in Figure 3.2. This is a mechanical tunable 3-D FSS; the reconfigurable characteristics are achieved by compressing the structure, thus changing both conducting and dielectric balls into disks with an increase in the surface area. The balls are firstly compressed into ellipsoids and then into flat disks. The rule of compression is: keep the volume of the each part (conducting, dielectric balls as well as the substrate) unchanged during the compressing procedure. The thickness of each substrate layer will decrease during the compression process. All the dimensions of the FSS are listed in Table 3.1. The size of the unit cell is 39.5 mm × 39.5 mm. Each layer of

the FSS has a thickness of 12 mm with a total thickness of 24 mm. The FSS is designed to be tunable in S band (from 2.60 GHz to 3.95 GHz).

Table 3.1 FSS unit cell dimensions-design iteration I

R_{cond}	V_{cond}	R_{die}	V_{die}	d_1	dx, dy	dx_1, dy_1
5 mm	5.24×10^{-7} mm^3	3.0 mm	1.13×10^{-7} mm^3	1 mm	19.75 mm	10.5 mm

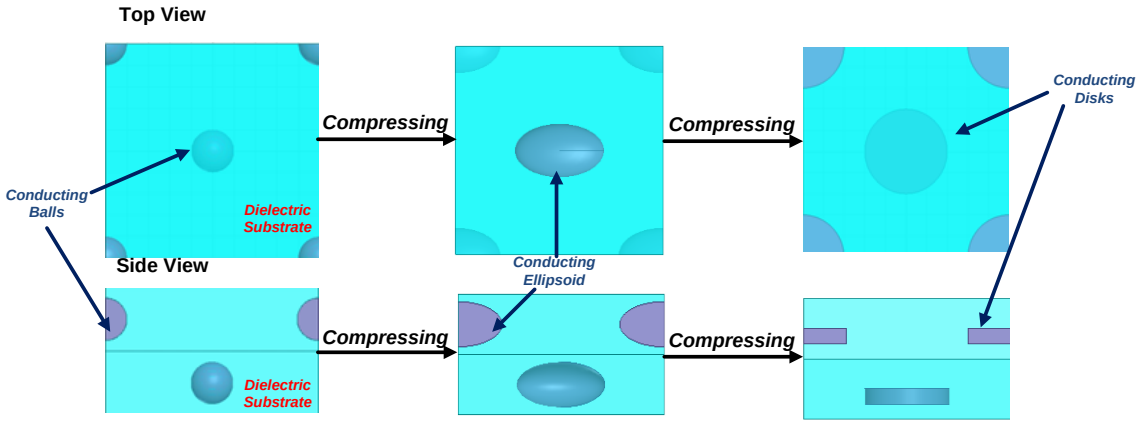

Figure 3.1 Compressible FSS unit cell-design iteration I

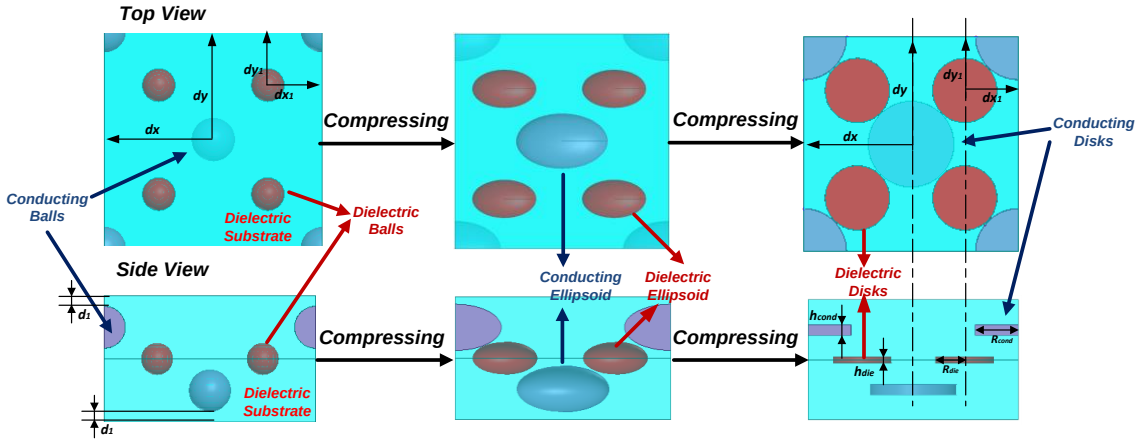

Figure 3.2 Compressible FSS unit cell with dielectric material-design iteration I

Conceptual Circuit Model

By arranging the unit cells periodically, the FSS will create a band-stop filter response in the S band. A crude conceptual circuit model of the unit cell is shown in Figure 3.3. The conducting balls/disks are modeled by inductors L_{cond} because they allow current to transfer between the top and bottom layer of the FSS. The tunable surface of conducting disks as well as the tunable substrate thickness could be modeled as a variable capacitor C_{sub}, the compressible dielectric disk can be model as a variable capacitor C_{die}. C_m represents the mutual capacitance between unit cells.

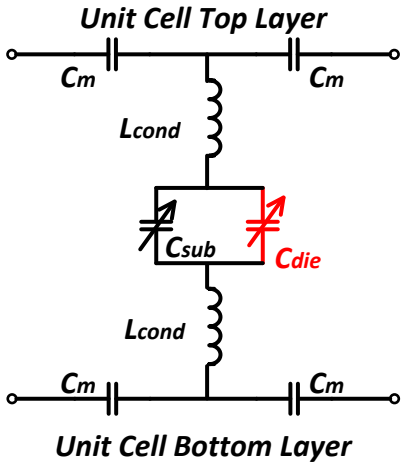

Figure 3.3 Conceptual circuit of the unit cell

The variable capacitance is in charge of the reconfiguration of the stop-band. The circuit resonates when the stored electric energy equals the stored magnetic energy at the frequency [20]:

$$f_0 = \frac{1}{2\pi\sqrt{2L_{cond}(C_{sub}+C_{die})}} \tag{3.1}$$

For the C_{sub} and C_{die}, they could be estimated from the parallel plate capacitor model,

$$C_{sub} = \varepsilon_0 \varepsilon_{sub} \frac{A}{d} \tag{3.2}$$

$$C_{die} = \varepsilon_0 \varepsilon_{die} \frac{A}{d} \tag{3.3}$$

Floquet Port Simulation

The FSS is simulated in HFSS as an infinite array. Master and Slave boundaries along with Floquet Ports create an infinite mirror boundary. Details of the setup in the

simulation can be found at [21]. Figure 3.4 shows the boundaries and Floquet port setup in HFSS.

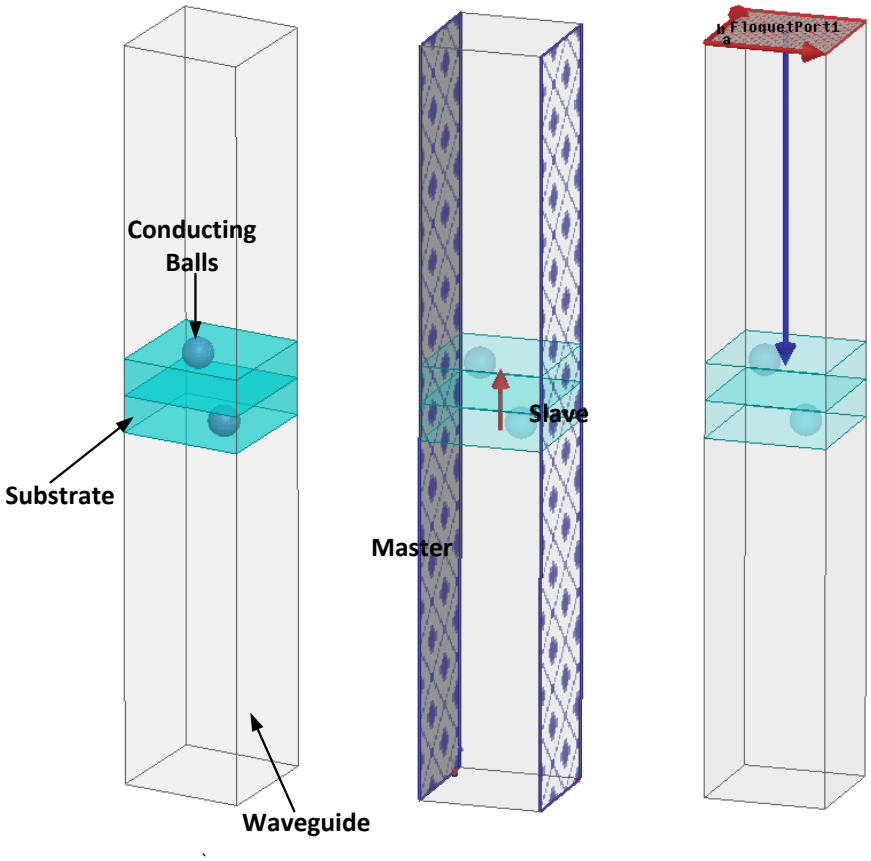

Figure 3.4 HFSS simulated infinite array with Master-Slave boundaries

A simulated transmission coefficient for infinite FSS is plotted in Figure 3.5. The resonant frequency is at 3.32 GHz for the initial uncompressed state with an incident angel of zero degree.

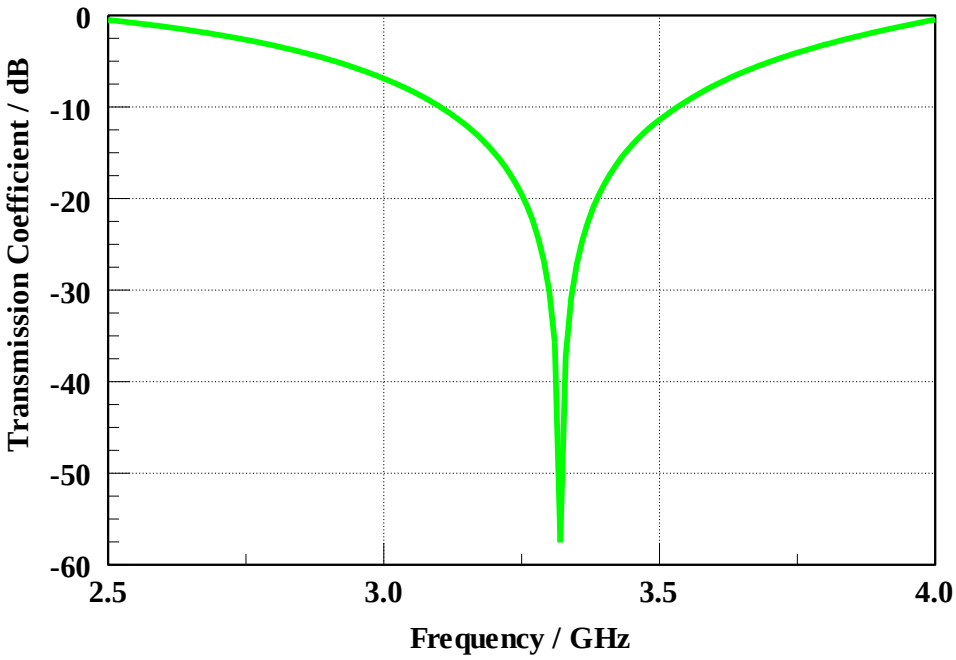

Figure 3.5 Transmission coefficient for FSS in initial ball state-design iteration I

FSS is a spatial filter that is not only subjected to the change of frequency but also deal with signals of various angles of incidence as well as polarization. This will typically cause some variations in the resonant frequency, the bandwidth as well as the transmission/ reflection performances. Figure 3.6 compares TE and TM polarization for the reconfigurable FSS. There is no difference in the transmission of the wave for TE versus TM due to a symmetrical geometry.

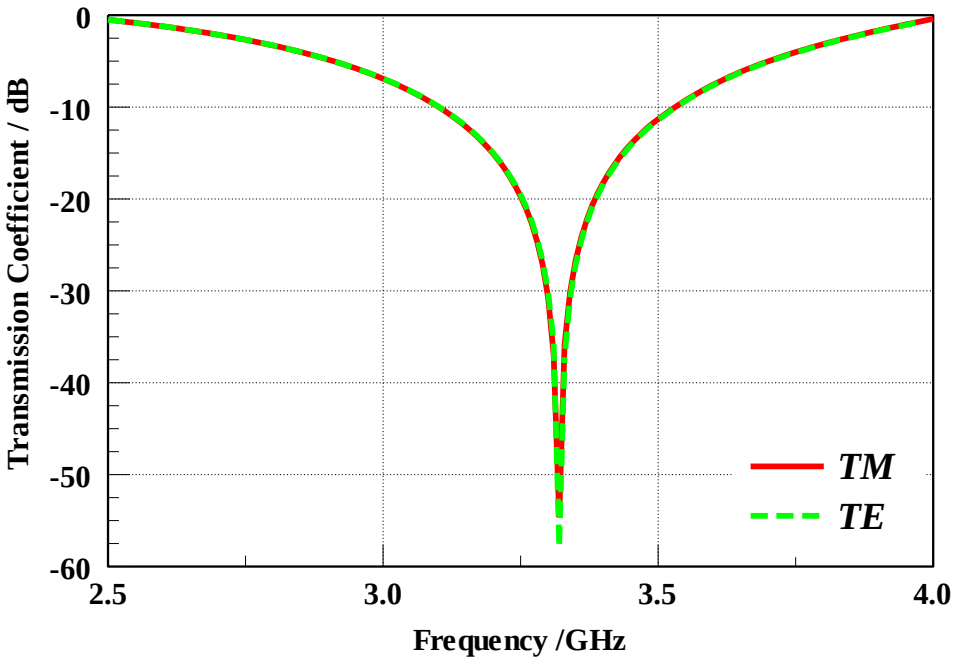

Figure 3.6 TE and TM polarization for the FSS

Multiple angles of incidence were also simulated by HFSS. The frequency response of the FSS changes with a widely varied incident angle of the incoming electromagnetic wave. With the incident angel changing from 0 degree to 60 degree, only a small frequency shift occurs, however, the incident angle larger than 60 degree will cause a huge influence on the response. Frequency response affected by the angle of incident is plotted in Figure 3.7.

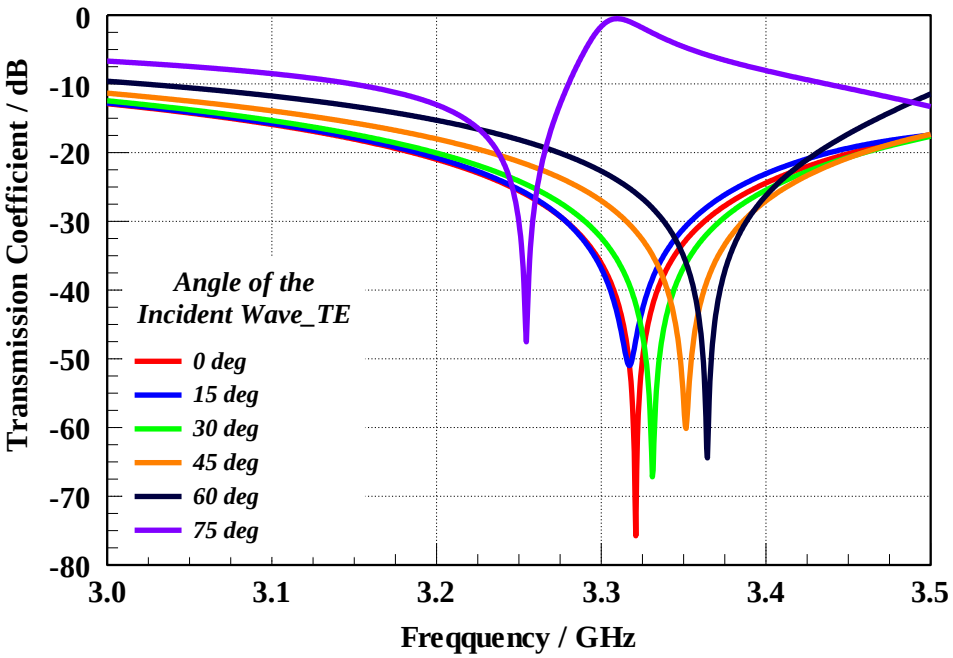

Figure 3.7 Transmission coefficients for multiple angels of incidence

The first reconfigurable FSS is simulated from initial conducting ball state to the compressed ellipsoid sate and then flat disk state for the model in Figure 3.1. Figure 3.8 is the HFSS simulations of the transmission coefficient in the ellipsoid state with a resonant frequency of 3.27 GHz while Figure 3.9 is the frequency response for flat disk state. The conducting disks' radiuses are swept from 6 mm to 10 mm, the resonant frequency shifts from 3.29 GHz to 3.14 GHz. A summary of the dimensions as well as the resonant frequencies are listed in Table 3.2. The resonant frequency during the whole compressing process is tuned from 3.32 GHz to 3.14 GHz.

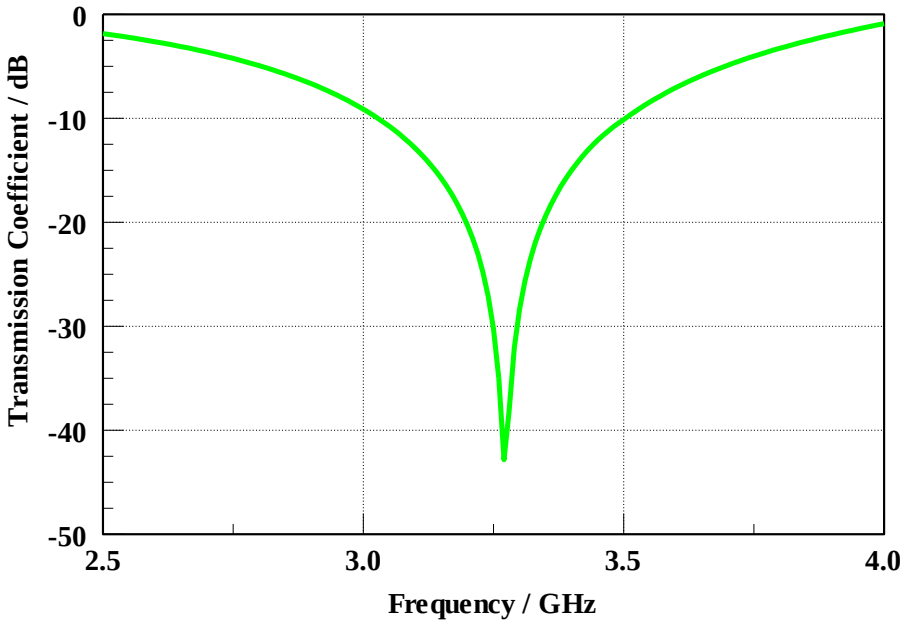

Figure 3.8 Transmission coefficient for FSS in ellipsoid state-design iteration I

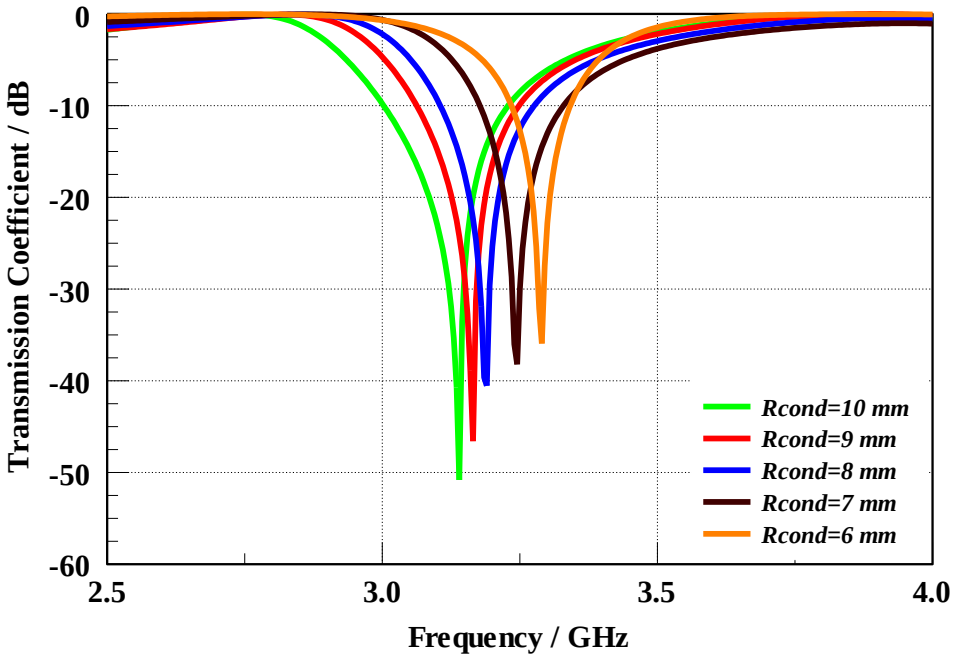

Figure 3.9 HFSS simulated transmission coefficients with conducting disk radius from 6mm to 10 mm-design iteration I

Another reconfiguration design is simulated for the model in Figure 3.2 with the addition of some dielectric material. First of all, an ellipsoid state was simulated with the dielectric, the transmission coefficient is plotted in Figure 3.10, and then the FSS is compressed into disk state. Since the dielectric balls' radius are 3 mm and they are compressed simultaneously with conducting balls with radius changing from 3.6 mm to 7 mm. A relative permittivity of 10 is used for the dielectric due to the most significant change in the resonant frequency and the material availability from the lab. Simulation results are plotted in Figure 3.11, the resonant frequency shifts from 3.18 GHz to 3.02 GHz. A comparison between the two cases: with and without dielectric objects is listed in Table 3.2.

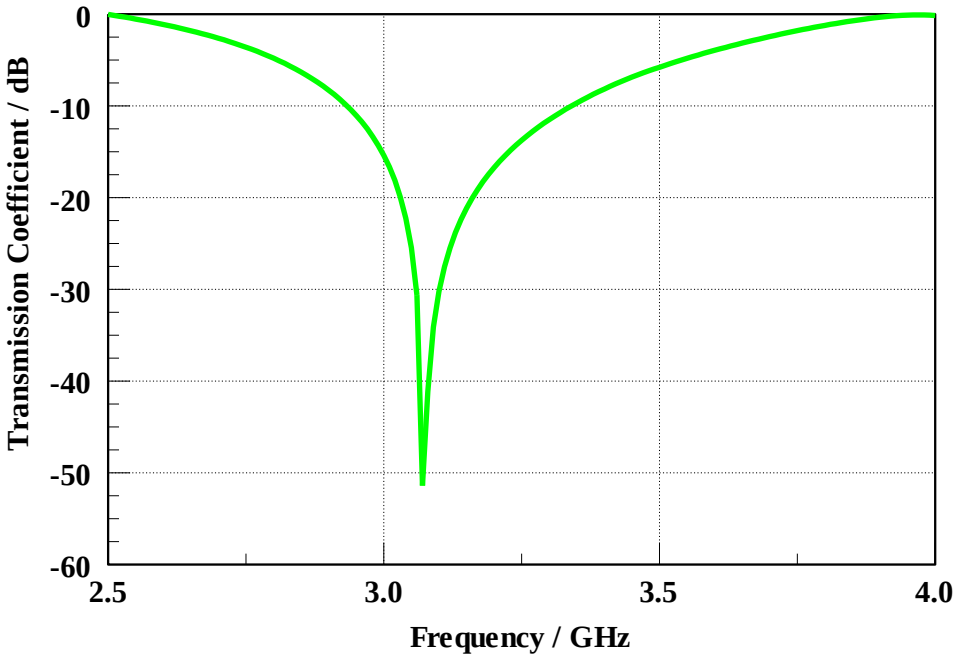

Figure 3.10 Transmission coefficient in ellipsoid state with dielectric-design iteration I

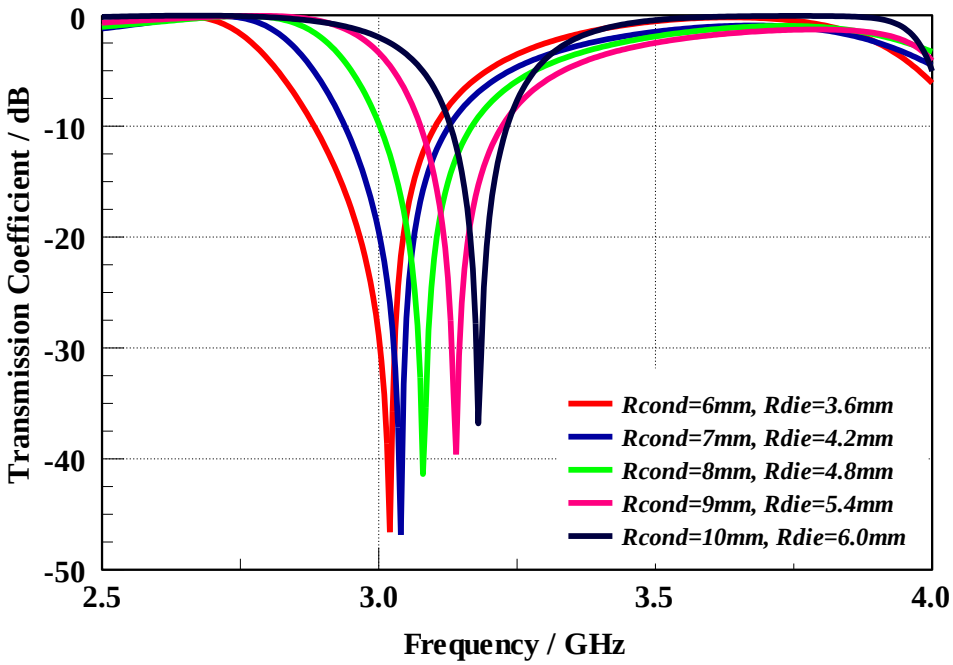

Figure 3.11 HFSS simulated transmission coefficients with conducting disk radius from 6mm to 10 mm, dielectric disk radius from 3.6 mm to 6 mm-design iteration I

Table 3.2 Comparison of reconfigurable FSS with/ without dielectric-design iteration I

Increment in radius	20%	40%	60%	80%	100%
Conducing disk radius/ mm	6	7	8	9	10
Conducting disk thickness/ mm	4.63	3.40	2.65	2.06	1.67
Dielectric disk radius /mm	3.6	4.2	4.8	5.4	6.0
Dielectric disk thinness/ mm	4.42	3.25	2.49	1.96	1.59
Resonant frequency without dielectric /GHz	3.29	3.25	3.19	3.17	3.14
Resonant frequency with dielectric /GHz	3.18	3.14	3.08	3.04	3.02

From the above results, we could get a conclusion that by adding the dielectric material for every single dimension, the resonant frequency decreases a little bit. This is due to the dielectric material has a higher dielectric constant than the substrate. This will add a C_{die} in the circuit model and will drop the resonant frequency based on Equation (3.1). With the increasing of the dimensions of the disks, the conducting surface area of the capacitor model is bigger, increasing the capacitance of C_{sub} and C_{die}, the resonant frequency will drop further. For the conducting disk case, the tuning range is around 180 MHz, while for the conducting and dielectric disks all together case, the tuning range is around 300 MHz.

Design Iteration II

The conducting balls (chrome balls used in prototyping) located at each corner of the top layer unit cell are difficult to cut so some changes have been made to make the design to be applicable for manufacturing and experimental testing. All the components have been moved along the horizontal plane in order to make the quarter balls at the corner placed inside the substrate, some dielectric balls have been eliminated to avoid the half/ quarter dielectric ball case at the edges. A plot in Figure 3.12 will help illustrate this movement as an infinite array.

The size of the unit cell remains 39.5 mm by 39.5 mm. The model of the compression of Design II is plotted in Figure 3.12 and Figure 3.13 as with/without dielectric case respectively. The thickness is the same as the first design. With

compression, the initial ball state as first changed into ellipsoid state and then flat disk state. Details of the dimensions of the new design are listed in Table 3.3.

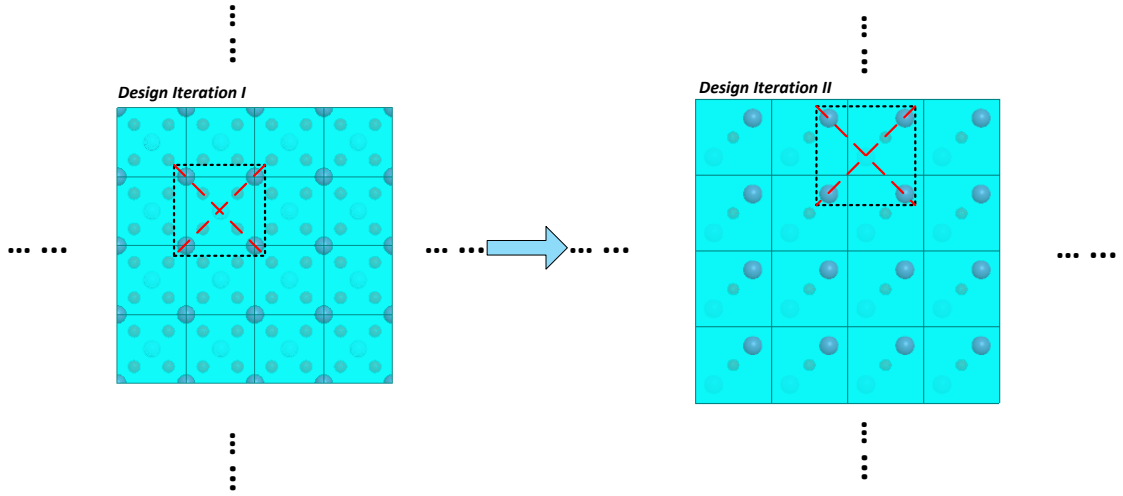

Figure 3.12 Design iteration change illustration

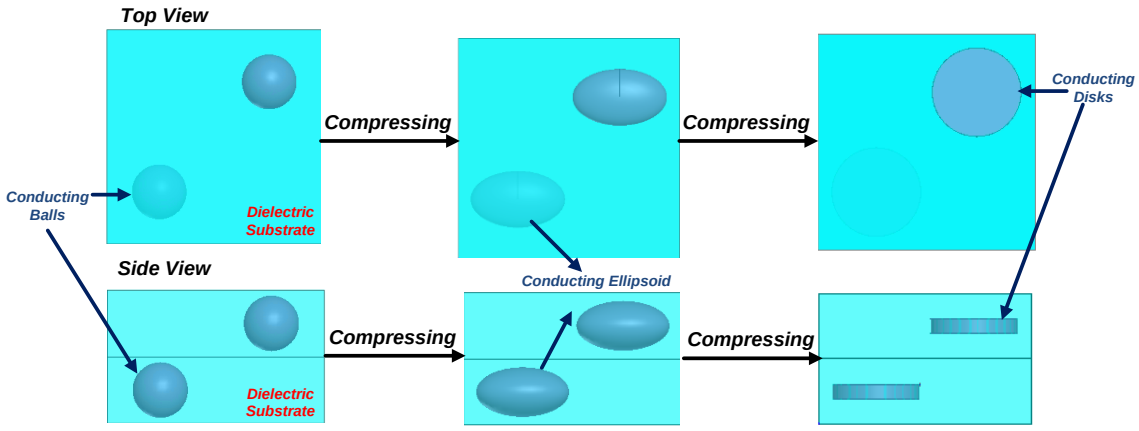

Figure 3.13 Compressible FSS unit cell-design iteration II

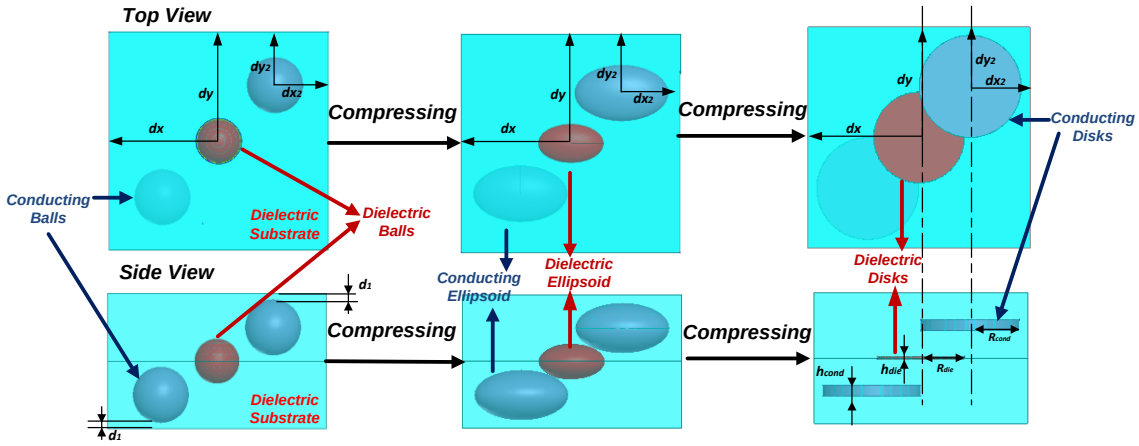

Figure 3.14 Compressible FSS unit cell with dielectric materiel-design iteration II

Table 3.3 FSS unit cell dimensions-design iteration II

R_{cond}	V_{cond}	R_{die}	V_{die}	d_1	dx, dy	dx_2, dy_2
5 mm	5.24×10^{-7} mm^3	3 mm	1.13×10^{-7} mm^3	1 mm	19.75 mm	10.5 mm

A simulated transmission coefficient for the infinite (simulated) FSS is plotted in Figure 3.15. The resonant frequency is 3.33 GHz for the initial uncompressed ball state with an incident angel of zero degree. This model has a very close transmission response as the first design iteration. Moreover, in this design, the response of the FSS is still independent of the polarization due to the symmetrical structure. A plot showing the angle of incidence is shown in Figure 3.16, as we can see the incident angle stability is not as good as the first design while the resonant frequency starts to shift from 60 degree.

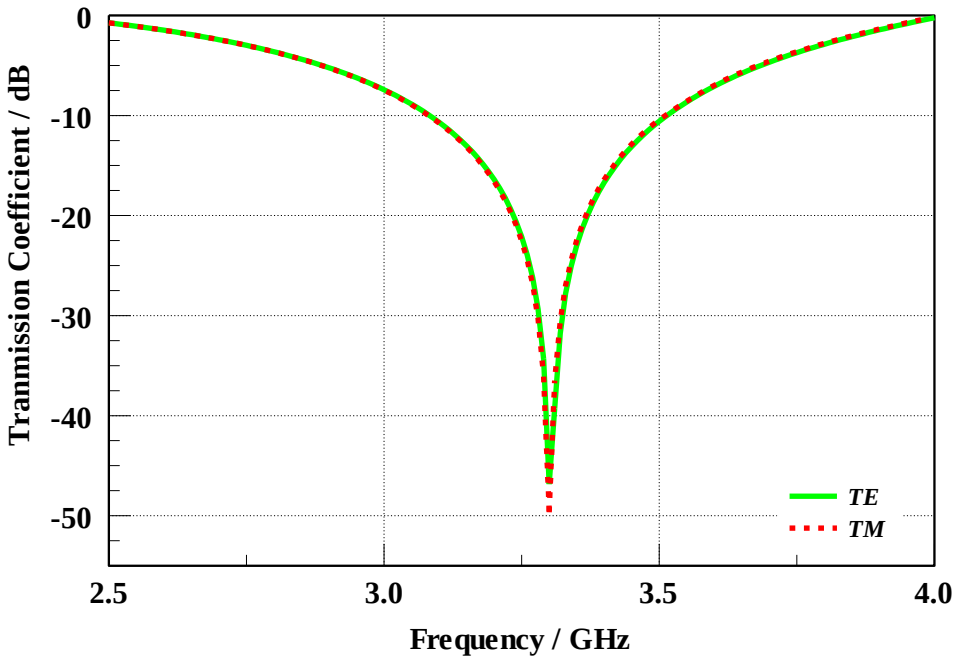

Figure 3.15 Transmission coefficient for FSS in initial ball state-design iteration II

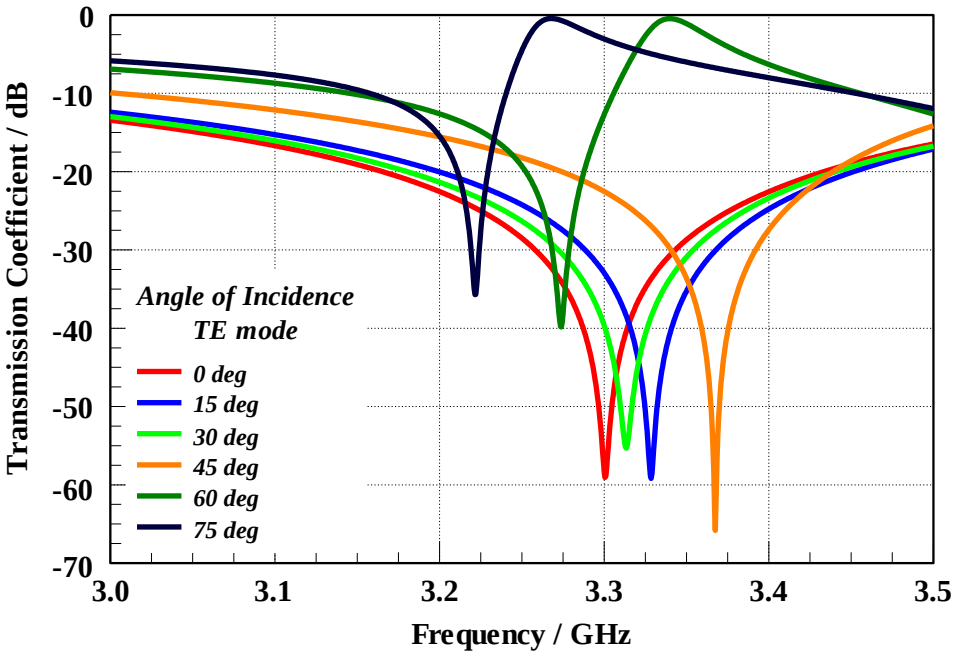

Figure 3.16 Transmission coefficients for multiple angels of incidence-design iteration II

The reconfigurable FSS is simulated from initial ball state to ellipsoid state and then compressed disk state similar to the first design iteration. Figure 3.17 is the HFSS simulations of the transmission coefficient in the ellipsoid state. Figure 3.18 is the conducting disk state, with the disks' radius are swept from 6 mm to 10 mm. This range is chosen due to the largest dimension of 10 mm that could fit in a FSS unit cell. The resonant frequency shifts from 3.23 GHz to 2.83 GHz in the disk state. A summary of the dimensions as well as the resonant frequencies are listed in Table 3.4. A total tuning range of 490 MHz has been achieved during the whole compressing procedure, which is much wider than the first design iteration.

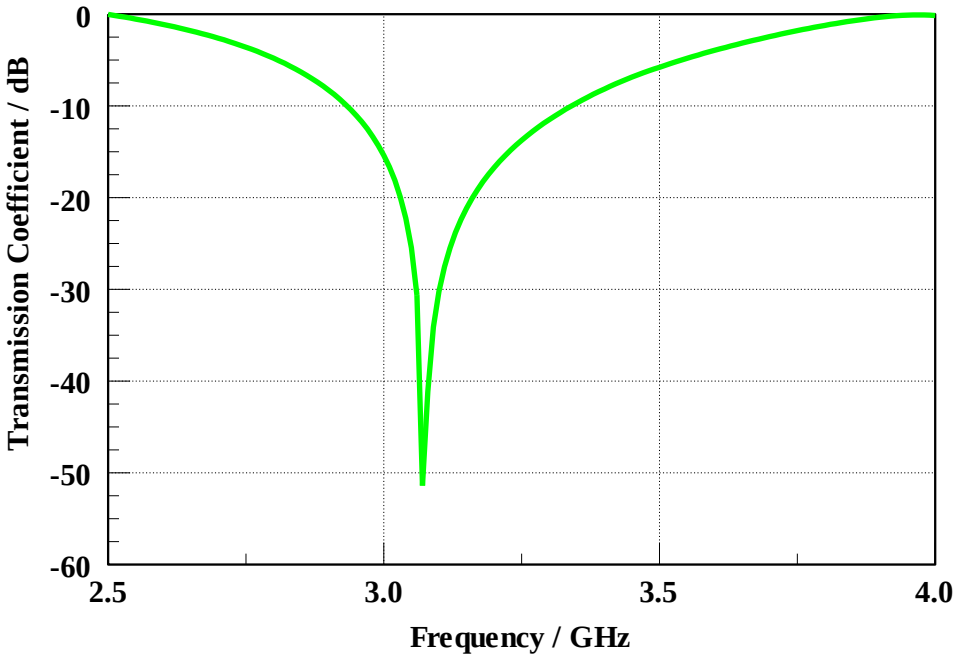

Figure 3.17 Transmission coefficient for FSS in ellipsoid state-design iteration II

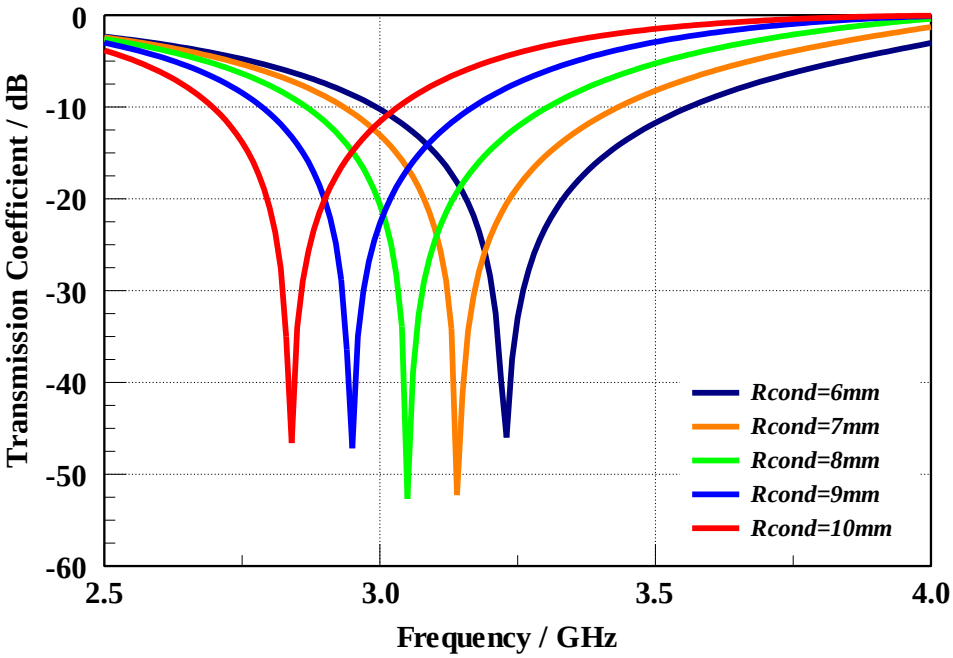

Figure 3.18 HFSS simulated transmission coefficients with conducting disk radius sweeping from 6mm to 10 mm-design iteration II

Table 3.4 List of disk dimensions with resonant frequencies

Disk radius (mm)	6	7	8	9	10
Disk thickness (mm)	4.63	3.40	2.65	2.06	1.67
Resonant frequency (GHz)	3.23	3.14	3.05	2.95	2.84

Form the plot and table above, it is clear that the resonant frequency is still inverse proportional to the radius of the disk. The explanation for this could be the same as the first design. When increasing the radius of the disks, in the same time decreasing the thickness, the capacitance of C_{sub} increases, resulting in a drop in the resonant frequency.

The reconfigurable FSS is then simulated by adding the dielectric objects, the relative permittivity ($\mathcal{E}_r$) of the dielectric material are taken into consideration in this design. $\mathcal{E}_r$ is swept from 1 to 10 in order to figure out its influence on the reconfigurable FSS. The range from 1 to 10 is chosen due to the availability of material that could be achieved in our lab. The simulated S_{12} parameters are plotted in Figure 3.19. In this case, a conducting disk radius of 6 mm with a dielectric disk of 3.6 mm is used as an example model.

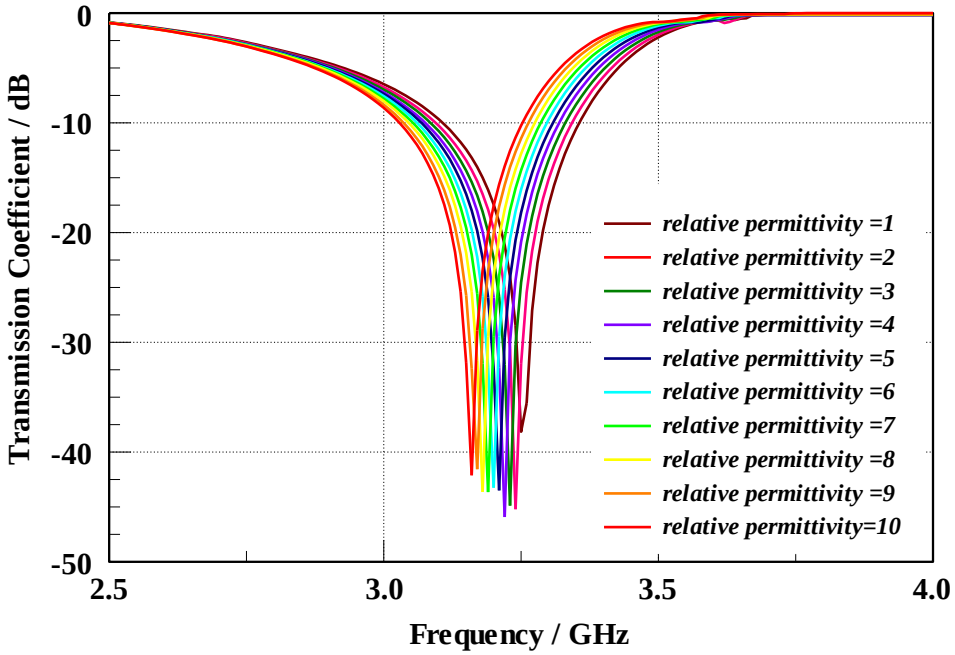

Figure 3.19 HFSS simulated transmission coefficients with various relative permittivity for the dielectric materials

The resonant frequency decreases with the increasing of dielectric relative permittivity. The relationship between them could be seen in Figure 3.20. The resonant frequency is inverse proportional to the dielectric constant, which shifts from 3.25 GHz

to 3.16 GHz with the $\mathcal{E}_r$ increasing from 1 to 10. This could be explained by Equation (3.1) and (3.3), with an increase in the dielectric constant, the variable C_{die} capacitance caused by the dielectric disks increases, this will make the resonant frequency smaller respectively. A relative permittivity of 10 is used in this work due to the most significant change in the resonant frequency.

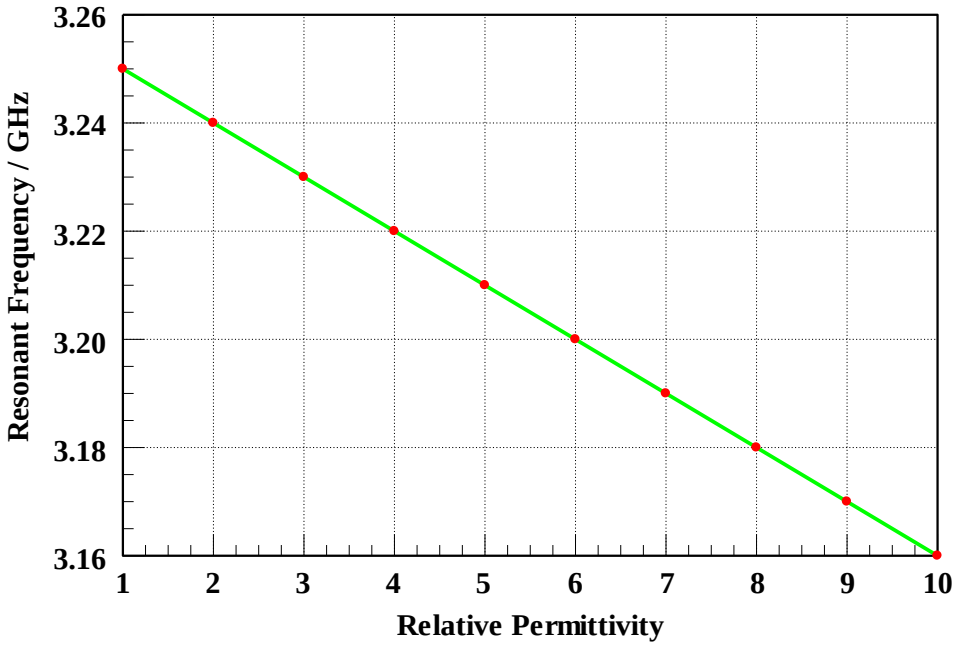

Figure 3.20 Resonant frequencies versus dielectric relative permittivity

By adding the dielectric balls into the structure and compressing the FSS. The FSS was firstly changed into the ellipsoid state and then the flat disk state. Figure 3.21 is the transmission coefficient in the ellipsoid state. For the disk state, the dielectric balls are pressed into disks to the same extend of the conducting balls. The simulated transmission coefficients are plotted in Figure 3.22. The conducting disks' radius was

swept from 6 mm to 10 mm, while the dielectric disks' changed from 3.6 mm to 6 mm. A comparison between the reconfigurable FSS resonant frequencies for with and without dielectric objects cases are shown in Table 3.5.

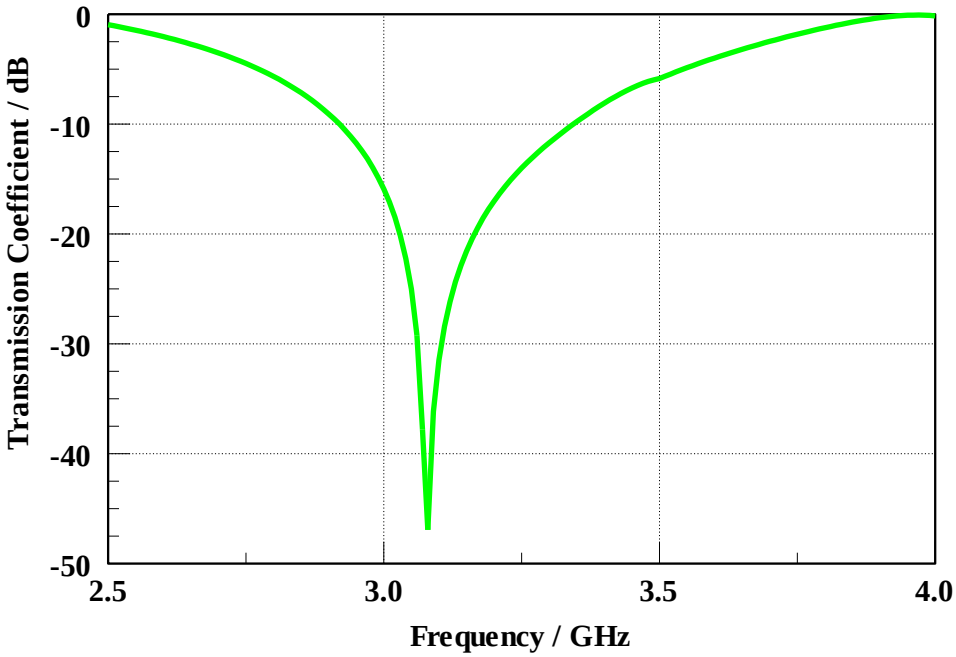

Figure 3.21 Transmission coefficient in ellipsoid state with dielectric -design iteration II

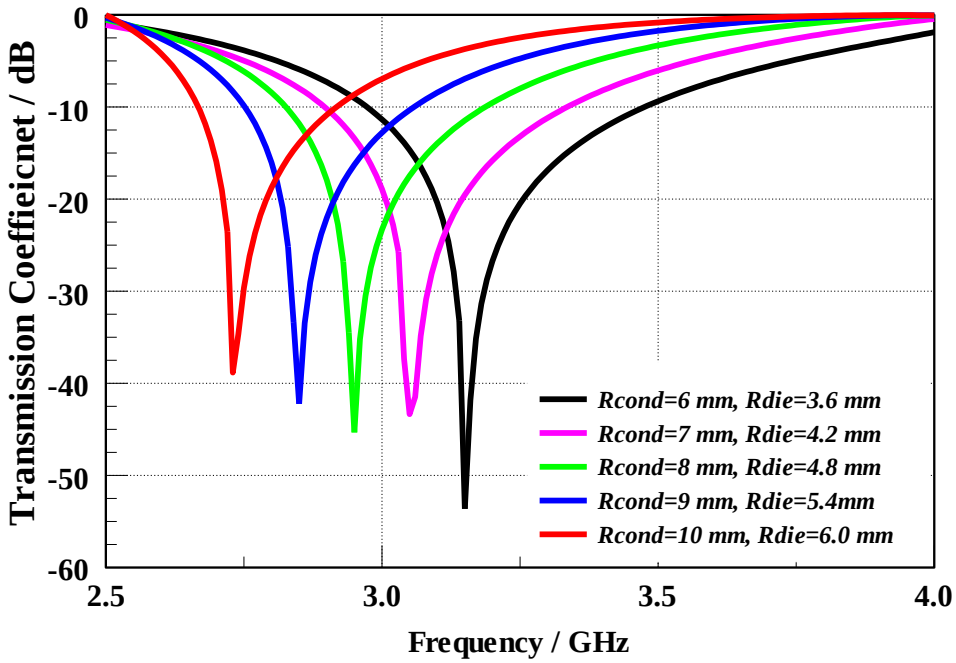

Figure 3.22 HFSS simulated transmission coefficients with conducting disk radius from 6mm to 10 mm, dielectric disk radius from 3.6 mm to 6 mm-design iteration II

Table 3.5 Comparison of reconfigurable FSS with/ without dielectric-design iteration II

Increment in radius	20%	40%	60%	80%	100%
Conducing disk radius/ mm	6	7	8	9	10
Conducting disk thickness/ mm	4.63	3.40	2.65	2.06	1.67
Dielectric disk radius /mm	3.6	4.2	4.8	5.4	6.0
Dielectric disk thinness/ mm	4.42	3.25	2.49	1.96	1.59
Resonant frequency without dielectric /GHz	3.23	3.14	3.05	2.95	2.84
Resonant frequency with dielectric /GHz	3.15	3.05	2.95	2.85	2.73

From the above table, we are able to conclude that, for the case without dielectric material inside; the total tuning range would be around 490 MHz. By adding some dielectric material inside, it could reach a tuning range of 600 MHz. Although in the second design iteration, the incident angle stability is not as good as the first one, it could be able to reach a wider tuning range than the first design.

CHAPTER IV

PROTOTYPE AND EXPERIMENT

Several sets of experiments were performed using a 2 by 2 unit cell array. The dimension for the surface under test is 79 mm by 79 mm, which is set by a square over-moded (expanded) S-band waveguide test fixture that is available for experiments. A square surface was chosen for this experiment to demonstrate the independence between TE and TM waves. Since a continuous compressing process is hard to control in the measurement, several prototypes of FSSs are made to represent the static tuning process.

FSS Prototype Fabrication

An array of 2 by 2 unit cells was fabricated for test in this work. This is determined by the available waveguide dimensions and the FSS unit cell structure. The prototypes were made by 3-D printer in the lab, because it could achieve a relative precise and stable fabrication process. 3-D printing technique is becoming popular in fabrication for microwave devices [22]. Unlike such traditional machining techniques which create the object by drilling or etching to remove and shape materials, 3-D printing generates three dimensional objects from a computer model by laying down successive layers of material. This not only addresses the alignment difficulties for the conventional printing applications but also provides endless opportunities for the fabrication of wide range of different EM (electromagnetic) structures.

Since a continuous compressing process is hard to control in the measurement, several prototypes of FSSs were made to represent the static tuning process. The substrate of the FSS is made of the PLA (Polylactic Acid), which is a common used filament for the 3-D printer. The FSS substrate was printed layer by layer in order to have the balls/disks inserted into substrate. Figure 4.1 shows the model of the four layers for fabrication.

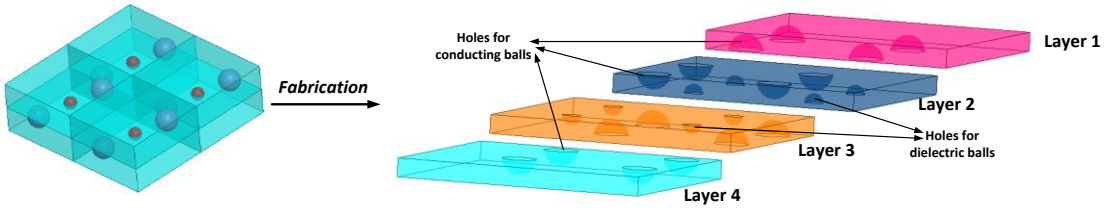

Figure 4.1 Layers for fabrication the FSS

For the ball case, chrome balls with radius of 5 mm and ceramic balls with a radius of 3 mm was used for building the FSS. The model in Figure 3.13 was fabricated, a picture of the fabricated model is shown in Figure 4.2 and the prototype of the model in Figure 3.14 with dielectric is shown in Figure 4.3. For the disk cases, aluminum disks with various radiuses were used, the manufactured prototype is shown in Figure 4.4. Moreover, Duroid 6010 with a thickness of 50mil are used for dielectric disks. Duroid 6010 has a dielectric constant of 10.2. Some Duroid disks are milled out by the milling machine in our lab. A figure of the prototype with dielectric disks is shown in Figure 4.5.

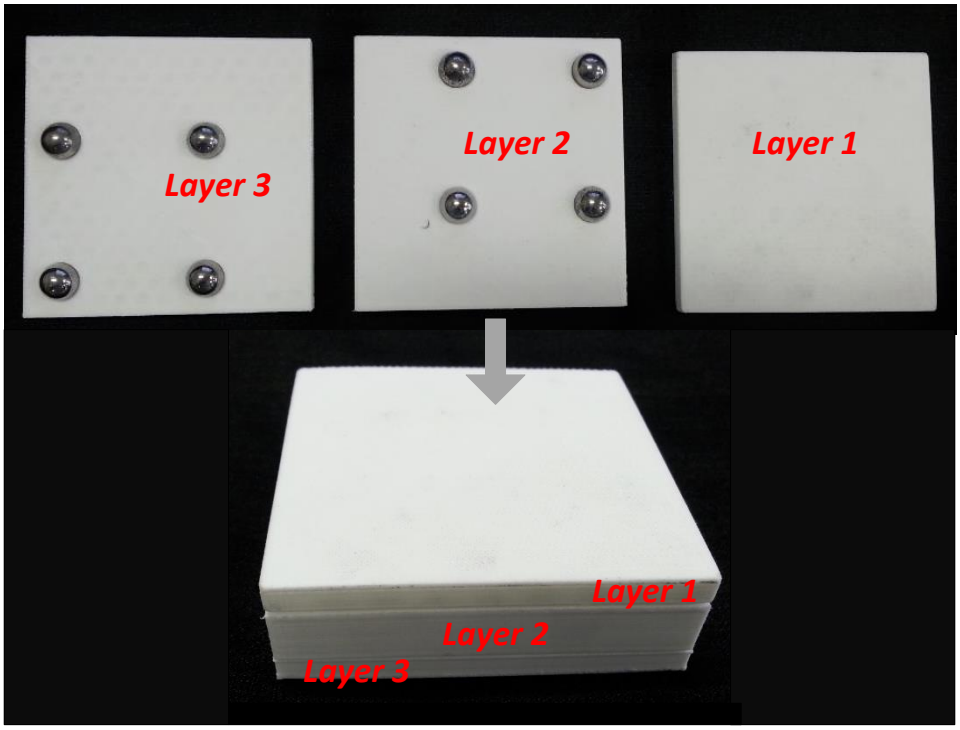

Figure 4.2 2 by 2 reconfigurable FSS with conducing balls

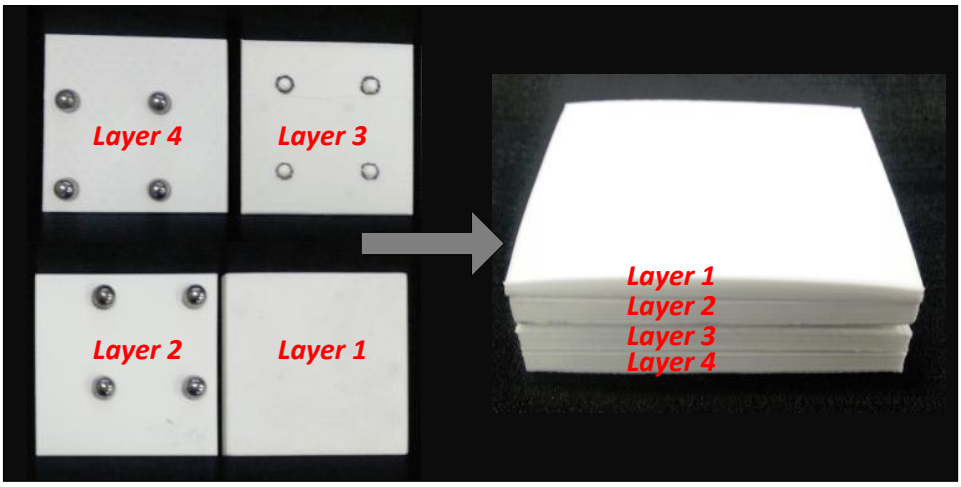

Figure 4.3 2 by 2 reconfigurable FSS with conducing and dielectric balls

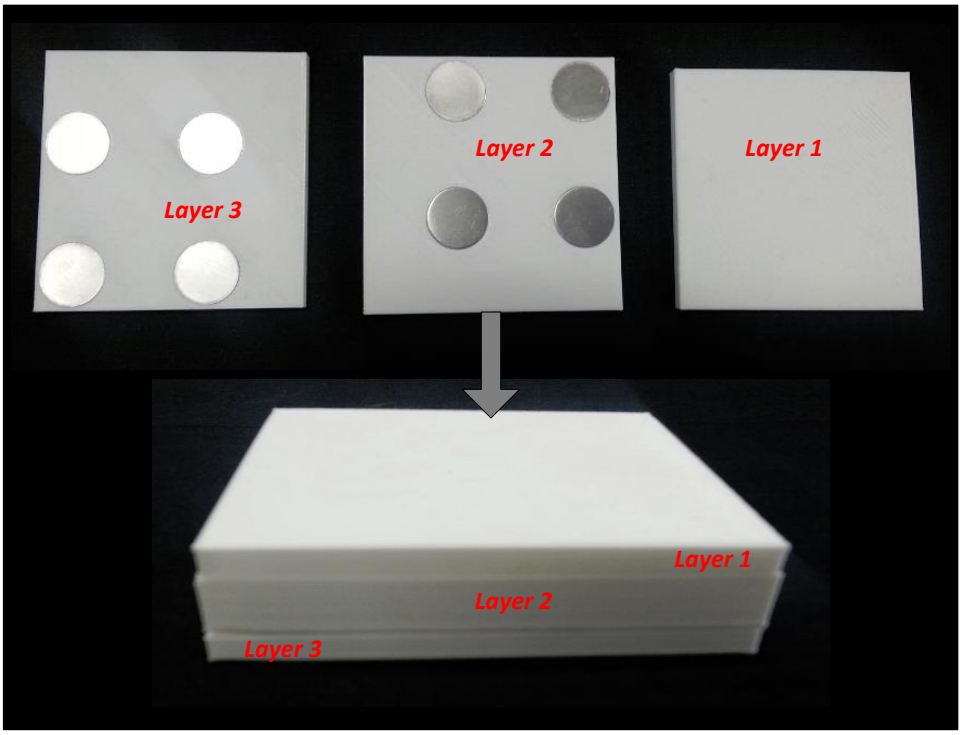

Figure 4.4 2 by 2 reconfigurable FSS with aluminum disks

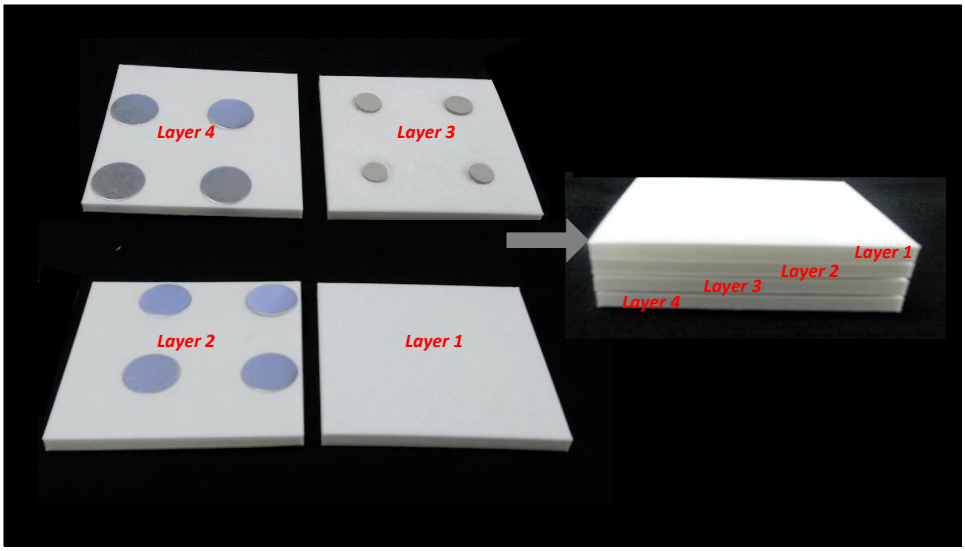

Figure 4.5 2 by 2 reconfigurable FSS with aluminum and Duroid disks

Experimental Setup

An expanded square waveguide was constructed for testing, which has same inner dimensions as the fabricated FSS: 79 mm by 79 mm. There are total two sections of the waveguide and each of them is 150 mm in length. The DUT is placed between the two sections of the waveguide and the waveguide is connected to the Agilent E8361C network analyzer. The setup for this experiment is shown in Figure 4.6.

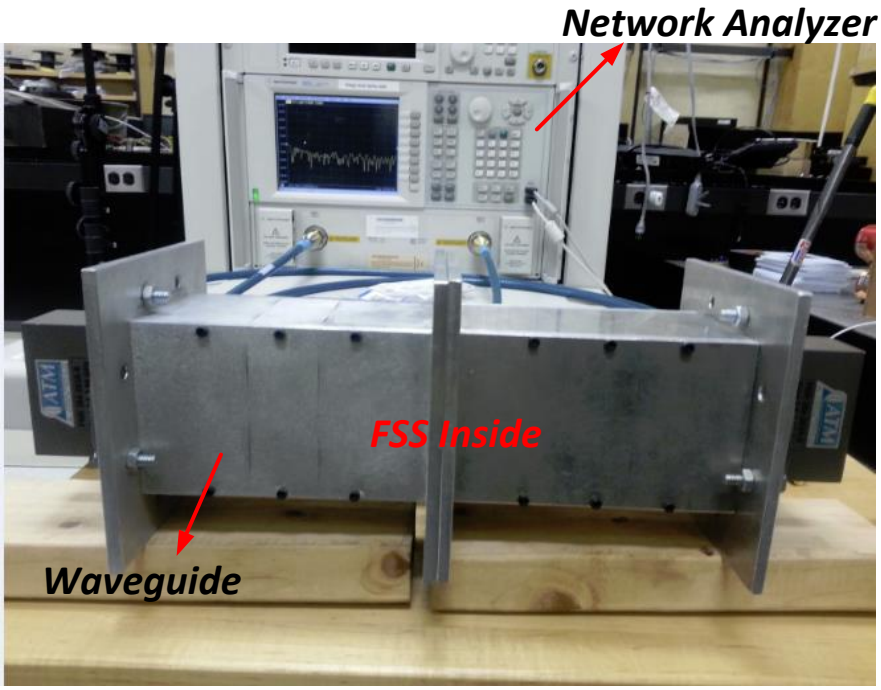

Figure 4.6 Test setup for the FSS

A TRL calibration was conducted first before testing the FSS to remove the unwanted iris and reflection and a measured S_{12} parameter after the calibration is shown in Figure 4.8. The TRL calibration is more accurate than an SOLT calibration, and this method is most often performed when the same connector type as the DUT is not

available. It does have another advantage that it is easier to manufacture and characterize three TRL standards than the four SOLT standards. The following standards were defined in our TRL calibration kit. A THRU standard of zero length, a REFLECT standard with a solid aluminum filling the aperture provide high reflection, and a LINE standard with the same dimensions as the waveguide aperture. The phase difference between the THRU and LINE should be greater than 20 degrees and less than 160 degrees over the frequency range. A picture of this TRL calibration kit is shown in Figure 4.7.

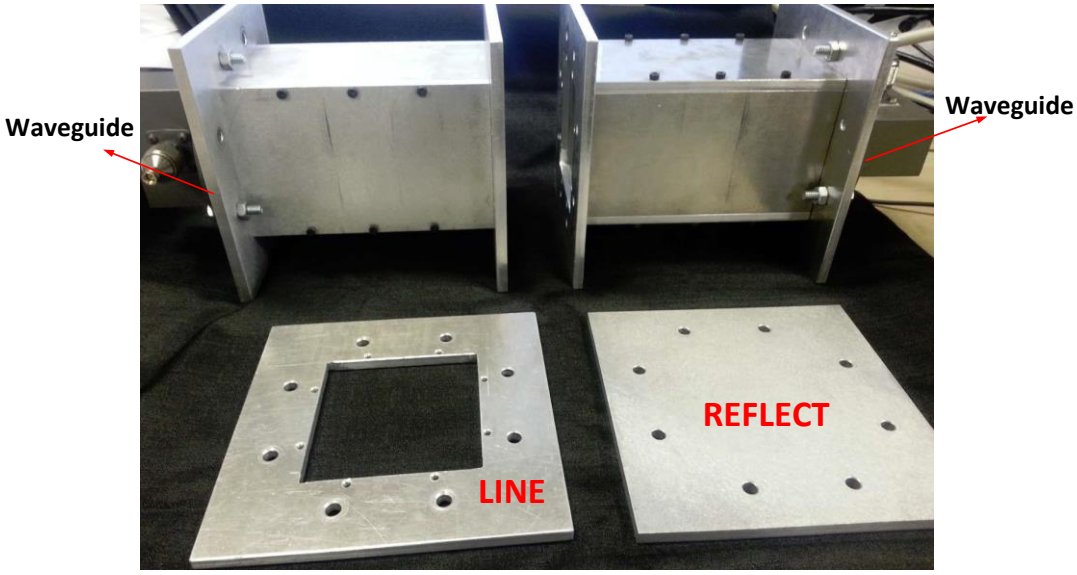

Figure 4.7 TRL calibration kit

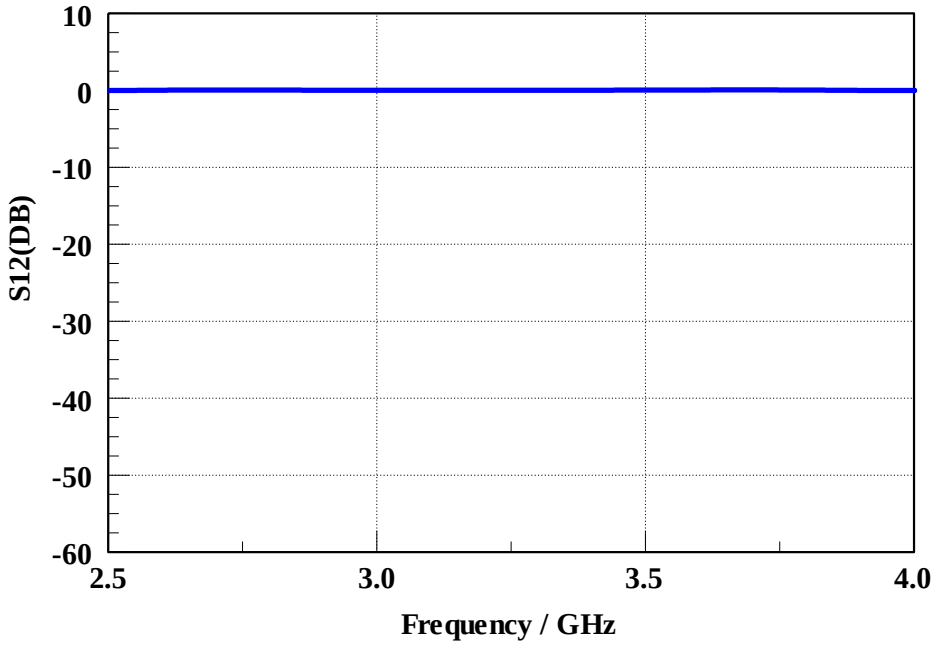

Figure 4.8 Measured S_{12} parameter after TRL calibration

Experimental Results

Gating is applied in the experiment, which provides the flexibility of selectively removing time domain responses. The remaining time domain responses can then be transformed back to the frequency domain. For reflection measurement, this feature helps move the effect of unwanted discontinues in time domain, while in the transmission measurement, this could help remove the effects of multiple transmission paths. Figure 4.9 shows the operation of gating.

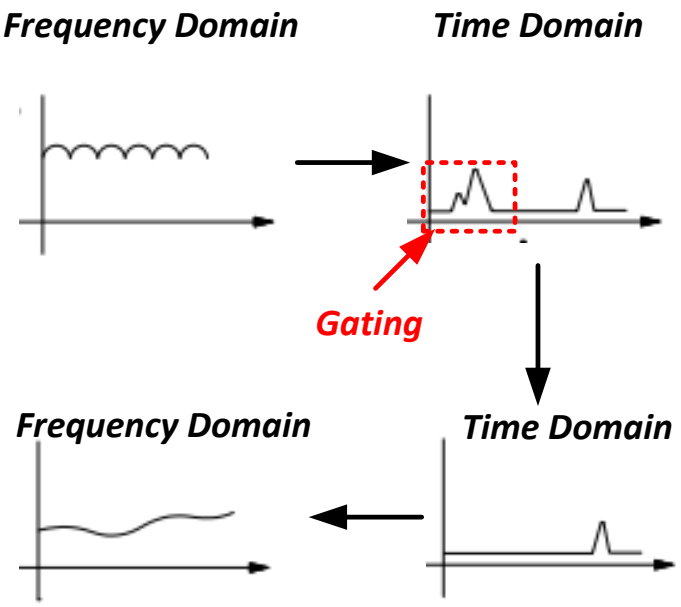

Figure 4.9 Gating operation

Gating could be considered as a band-pass filter in the time domain, the gate position is entered as a start/stop time or center/span time. The start and stop times are the band-pass filter -6 dB cutoff times. In this experiment, gating is added with a range around ±5 ns for different cases.

The 2 by 2 FSS has been measured by network analyzer following the above setup. The first measurement is taken for the uncompressed FSS in the ball state without the dielectric. The resonant frequency is about 3.79 GHz. Another test is conducted for the FSS with both chrome ball and ceramic balls inside, and the resonant frequency is about 3.75 GHz. The experiment results for these two cases are plotted in Figure 4.10 and Figure 4.11 respectively. More ripples appeared in the second graph may be due to the increasing of uneven layers and air gap between them.

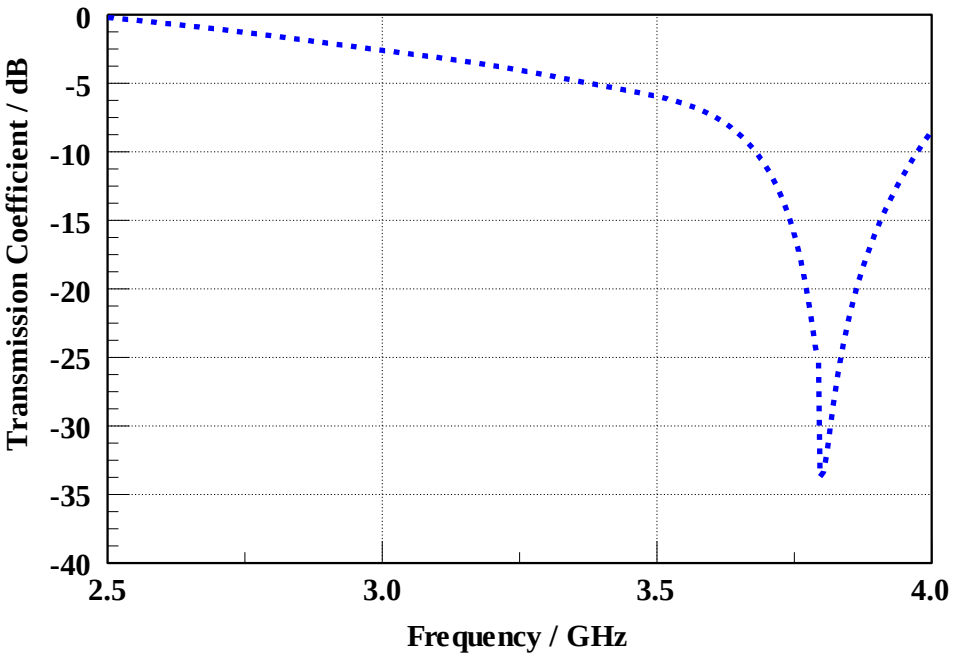

Figure 4.10 Measured S_{12} parameter for the ball state

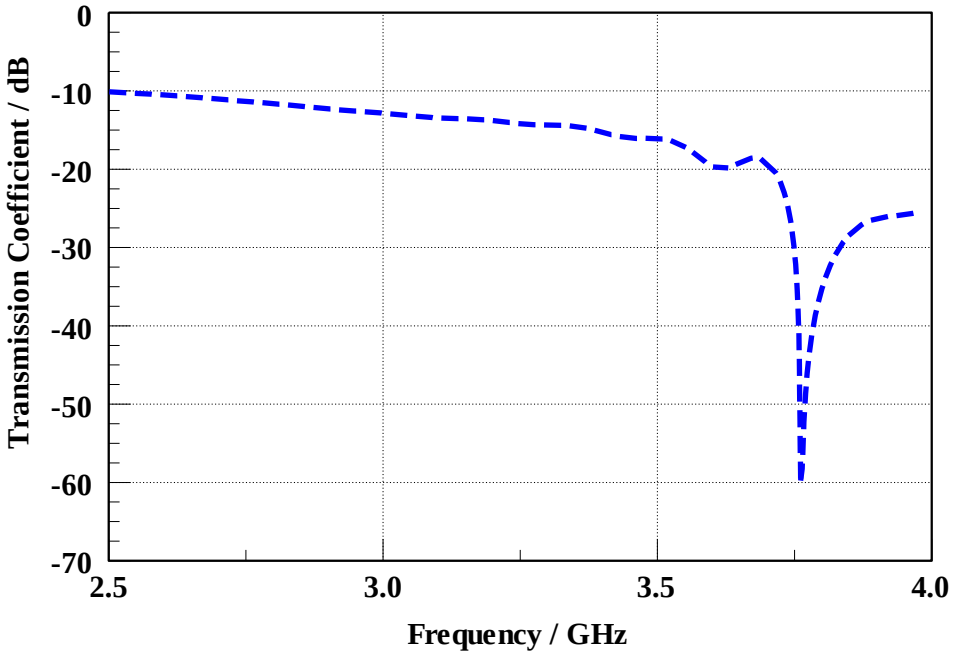

Figure 4.11 Measured S_{12} parameter for the ball state with dielectric

More tests have been conducted on the disk state with, three different types of aluminum disks are used as listed in Table 5.1, the measurement results are plotted in Figure 4.10. Furthermore, the prototypes with the dielectric disks are fabricated and the measurements on these prototypes are plotted in Figure 4.12 and Figure 4.13 respectively.

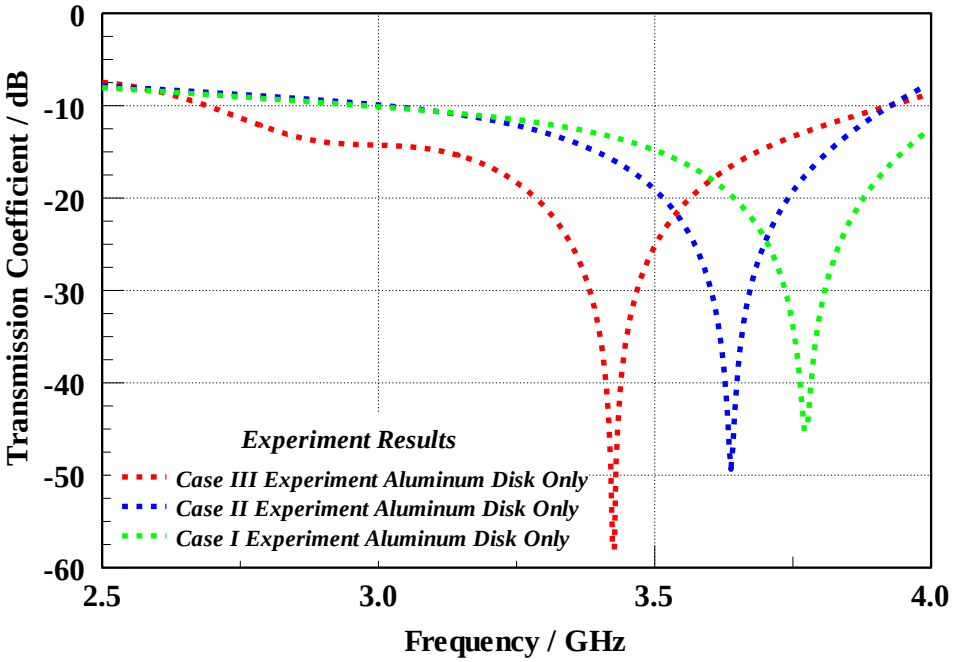

Figure 4.12 Measured S_{12} parameter for the disk state

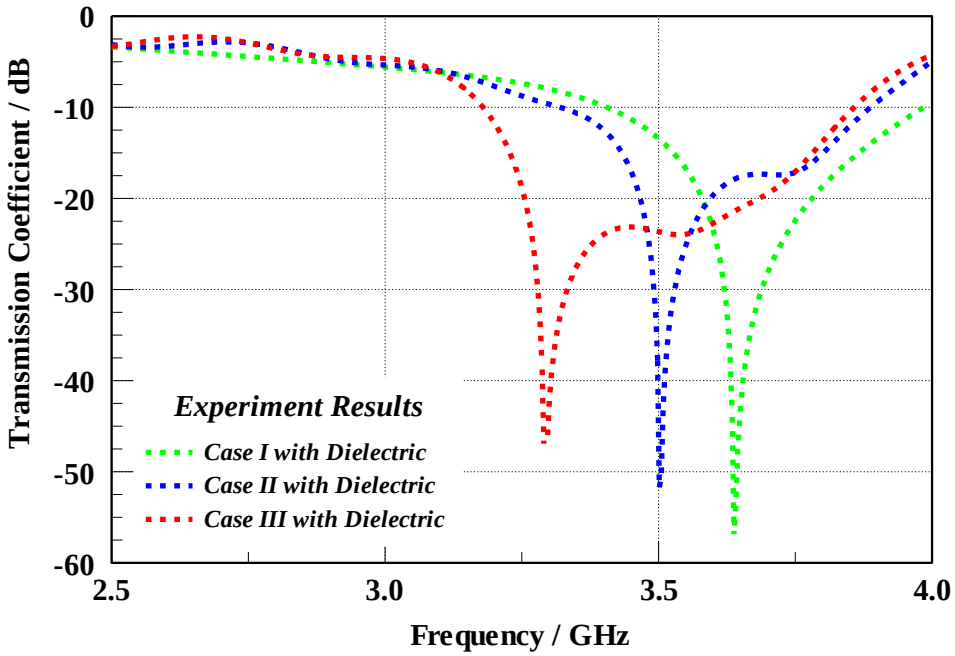

Figure 4.13 Measured S_{12} parameter for the disk state with dielectric

CHAPTER V

DISCUSSION

Several issues that need to be considered for the practical design are discussed in this chapter. These include: the properties of the available material for the experimental prototype, errors and losses that are caused during the manufacturing process and so on. More simulations are presented here for the prototype being built in order to predict the practical performance. Comparison between the simulations and the experimental results are discussed afterwards.

Material Properties

Polylactic Acid (PLA) is one of the most commonly used 3-D printing materials. It has the virtue of being both odorless and low-warp, so that it is used in a broad range of printing applications. The electrical properties of PLA have been investigated in [23]. From this paper, a measurement of the complex permittivity of and the conductivity of the PLA was taken in the frequency range from 10 mHz to 10 MHz, and the complex permittivity of the PLA is almost independent in this frequency range. At 50 Hz, the PLA has the following properties: dielectric constant 3.0, dielectric loss 0.022 and volume resistivity 49×10^{16} Ωcm. We will keep this property as a reference when using the PLA for the FSS substrate in this work. The dielectric constant of the substrate is not only depends on the relative dielectric permittivity of the PLA itself, but also depends on the infill percentage in the 3-D printing setup. The 3-D printed model is not 100% solid,

so that the overall dielectric constant of the substrate should be less than that of the PLA alone. The infill percentage is in control of the porosity of the substrate, shown in Figure 5.1. With a higher infill percentage, more PLA will be applied in the model, result in a higher dielectric constant.

Figure 5.1 Porosity of the printed PLA with 10% infill

For different infill setup in the fabrication, the dielectric constant of the substrate varies. In the previous design process in Chapter III, substrate was simulated as a plexiglass in HFSS with a relative permittivity of 3.4. In order to analyze the sensitivity of the FSS performance to the substrates' properties as well as how the PLA infill percentage will affect the overall dielectric constant, a simulation was conducted with substrate's dielectric constant sweeping from 2.4 to 3.2, loss tangent of 0.01 in HFSS. This simulation was using the initial uncompressed ball state model. The results are

shown in Figure 5.2. A figure of the resonant frequency versus the dielectric constant is plotted in Figure 5.3.

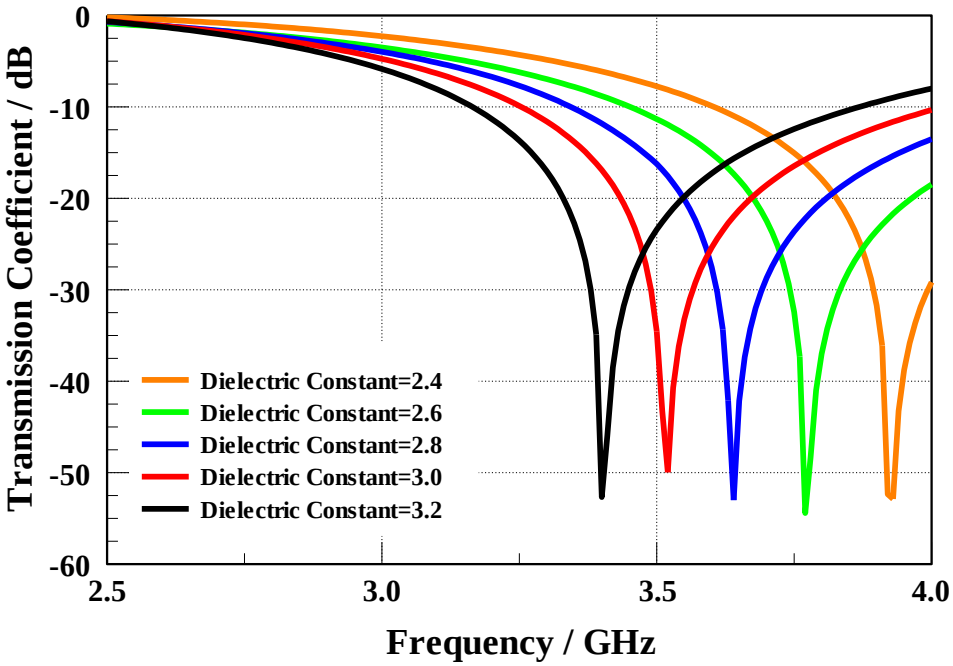

Figure 5.2 PLA dielectric constant sweep

From the plot above, it is obvious to see that, the resonant frequency of the FSS is very sensitive to the substrate's dielectric properties, so that this needs to be carefully considered in the practical design. More simulations based on the practical material properties will be provided below.

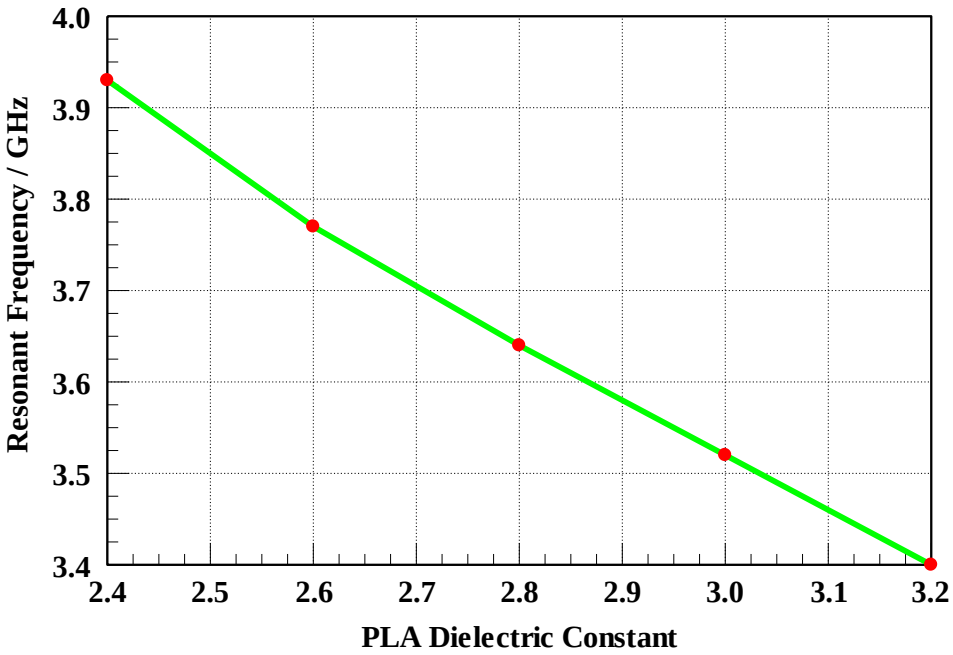

Figure 5.3 Resonant frequencies versus the dielectric constant

Errors and Losses

The performance of the reconfigurable FSS was influenced by errors and losses during the fabrication process. Two main errors are induced. One is from the conducing and dielectric components themselves, while the other is from the 3-D printer. Losses may exist in the materials being used and the air gaps are induced in the assembly of the FSS prototype.

Due to the limit components availability, the disks we could get from the lab are not in the exact dimensions as the simulations in design. Disk sizes as well as the disk thickness may vary. Several types of aluminum disks were ordered with the following dimensions to demonstrate the tuning of FSS. The measured dimensions are listed in Table 5.1.

Table 5.1 List of Aluminum disks dimensions

	Aluminum Disk1	**Aluminum Disk 2**	**Aluminum Disk 3**
Aluminum disk radius / mm	6.41	7.98	9.60
Aluminum disk thickness / mm	1.02	1.06	1.08

For the errors from the 3-D printer, since the 3-D printer has a highest resolution of 0.1 mm, this will cause some replacement of the inserted components and misalignment between the layers. It also has a normal problem of warping, the FSS surface is not flat enough, and so that air gaps exist between layers. This problem will become even worse when increasing the infill percentage. So that, each time before printing a new model, levelling the build plate becomes very necessary.

Simulations Based on Practical Issues

The FSS was re-simulated in HFSS after the first experiment are performed. According to the previous designs in our lab, with an infill of 30%, the PLA was simulated with a relative permittivity around 2.6, loss tangent of 0.01. The conducting balls were simulated by chromium material while the dielectric balls were simulated by Al_2O_3 ceramic. Blocks of air with thickness of 0.1 mm were included between the FSS layers. The simulation result is plotted in Figure 5.4. The resonant frequency has shifted to 3.77 GHz.

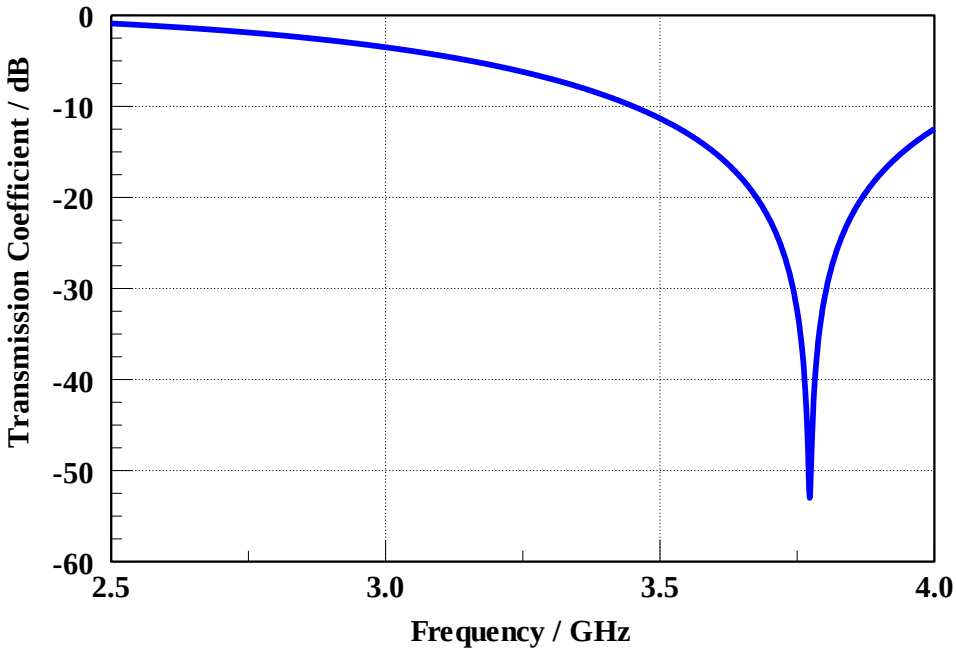

Figure 5.4 S_{12} with practical material properties for the ball state

More simulations have been done based on the available aluminum plates and the corresponding Duroid disks listed in Table 5.2. In order to keep the rule of compression mentioned in Chapter III: total conducting and dielectric volume should not be changed. Multiple layers of aluminum plates are used in order to keep the volume in each case as close as possible. Table 5.2 has listed all the dimensions for the practical design and the simulated transmission coefficients based on these for the conducting case is plotted in Figure 5.5 and the situation containing both conducting and dielectric disks are plotted in Figure 5.6.

Table 5.2 Practical design dimensions

		Increment in radius	Radius (mm)	Thickness (mm)	Number of Layers	Total Volume (mm^3)
Ball Case	Chrome Ball	--	5.00	--	--	523.60
	Ceramic Ball	--	3.00	--	--	113.10
Case I	Aluminum Disk	28.2%	6.41	4.08	4	526.39
	Dielectric Disk		3.85	2.42	2	111.70
Case II	Aluminum Disk	59.6%	7.98	2.12	2	426.04
	Dielectric Disk		4.80	1.22	1	88.26
Case III	Aluminum Disk	92.0%	9.60	1.08	2	578.75
	Dielectric Disk		5.76	1.09	1	113.56

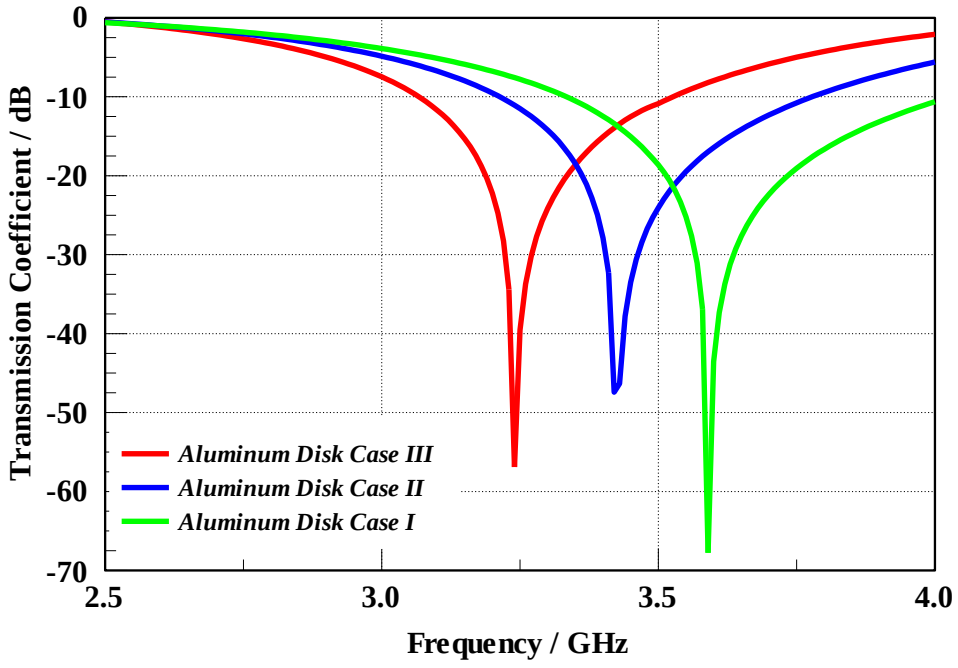

Figure 5.5 S_{12} with practical material properties for the conducting disk state

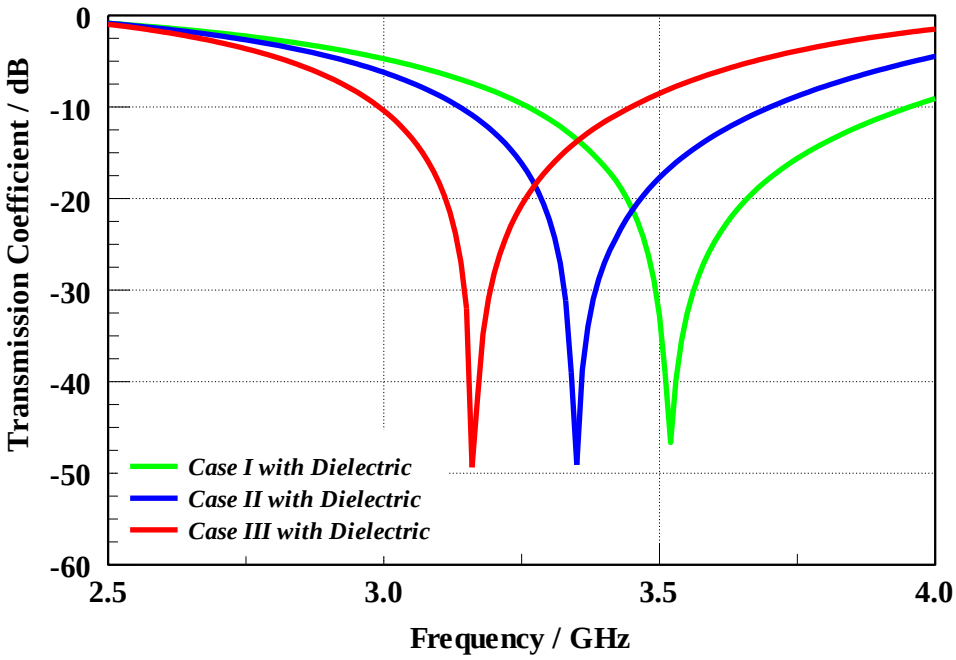

Figure 5.6 S_{12} with practical material properties for the disk state with dielectric

From Figure 5.5 above, by varying the disk radius from 6.41 mm to 9.60 mm, the resonant frequency of the stop-band shifts from 3.59 GHz to 3.24 GHz. The tuning range is about 350 MHz. From the initial ball state to the disk state, a maximum tuning range of 480 GHz could be achieved. From Figure 5.6, the minimum resonant frequency could be achieved at 3.16 GHz; so that this case would have a wider tuning range of 560 MHz could be achieved for the dielectric case. Table 5.3 lists the simulation results for the practical design for with/ without dielectric cases.

Table 5.3 Comparison of reconfigurable FSS with/ without dielectric-practical design

	Case I Resonant Frequency (GHz)	**Case II Resonant Frequency (GHz)**	**Case III Resonant Frequency (GHz)**
Aluminum Disks Only	3.59	3.42	3.24
Aluminum& Duroid Disks	3.52	3.35	3.16

Comparison between Simulations and Experimental Results

The first experiment results are plotted in comparison with the practical ball state simulation shown in Figure 5.7. There is a good match at the resonant frequency, the HFSS simulation is at 3.77 GHz and the experiment result is at 3.79 GHz. Figure 5.8 shows the comparison in the ball state with dielectric balls inside, the simulation has a resonant frequency of 3.76 GHz while the test reaches a resonant frequency around 3.75 GHz. However there are more ripples and losses in the second case than the first one, this might due to the second case has one more PLA layer than the first one in order to fit the dielectric balls inside and that uneven surface will cause these ripple coming up.

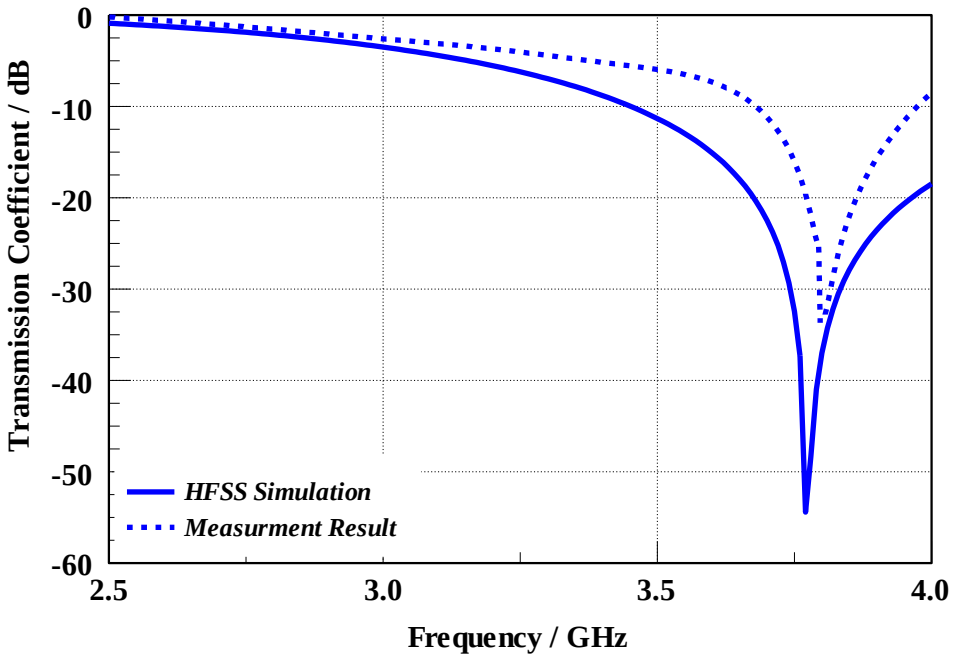

Figure 5.7 Comparison between measurement and simulation for the ball state

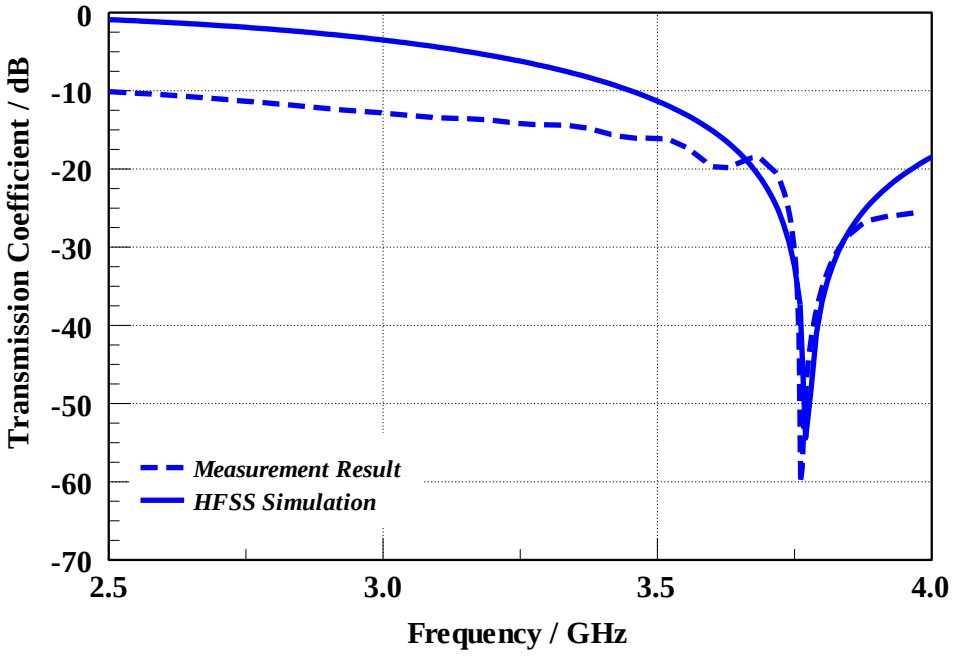

Figure 5.8 Comparison for the ball state with dielectric

More measurements have been done for the three aluminum disks listed in Table 5.2 with the practical design dimensions. The comparisons between HFSS simulations and the measurements are plotted in Figure 5.9 and Figure 5.10 for the conducting disk only case and with dielectric disk case respectively.

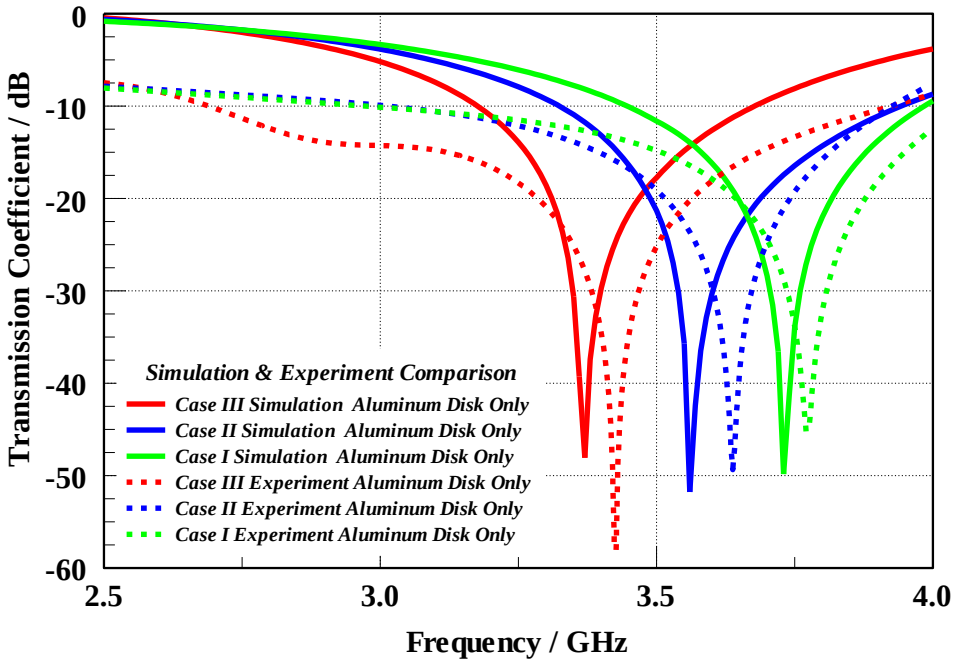

Figure 5.9 Comparison between measurement and simulation for the disk state-conducting disks only

From the plot below, there is around 50 MHz shift between the simulation and measurements, this might due to the PLA does not have an accurate relative permittivity that has been verified to be used in the simulation. In addition to this, the FSS is very sensitive to the substrate's properties according to the analysis above, so that, the estimation value for the dielectric constant used in the simulation is still a little bit higher than the exact value, causing a mismatch in the measurement. However, from the

transmission coefficient shape comparison, they are in a good match with a good calibration process. For the dielectric cases plotted in Figure 5.10, the same problem occurs.

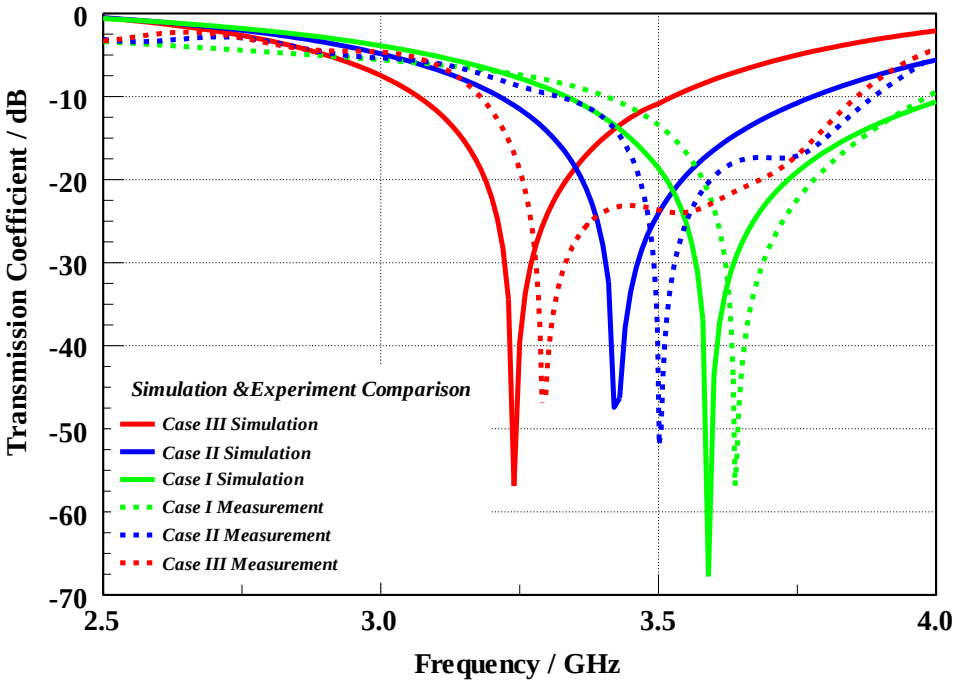

Figure 5.10 Comparison between measurement and simulation for the disk state-conducting & dielectric disks

CHAPTER VI

CONCLUSION

Summary

The 3-D compressible FSS demonstrated in this work provides TE and TM independence as well as the operation over a certain angels of incidence. Continuous reconfiguration characteristic is able to be achieved by mechanically compressing the 3-D structure without adding any electronic component. Stop-band response is presented and the resonant frequency of the stop-band can be tuned by varying the height of FSS as well as the surface area of the conducing components simultaneously during the compression process. In addition to this, by adding some dielectric material inside the FSS, a wider tuning range could be achieved. This reconfigurable FSS could be applied for a variety of applications, and the non-wired tuning mechanism provides the ability to reduce undesired radiation and reactive loading in use with antennas and other electromagnetic applications.

Two design iterations have been provided and the second iteration is able to be fabricated. Some prototypes of the FSS have been manufactured by 3-D printer in order to demonstrate the design. Static tests reveal the capability to control resonant frequency of the stop-band through varying the surface area conducing and dielectric components and the height of the structure during the compression. The fabricated FSS is a 2 by 2 array in order to fit for the S-band waveguide aperture and tested by the network analyzer. The initial state has a resonant frequency around 3.33 GHz, and this drops to

2.73 GHz with a double surface area compared to the initial state, the resonant frequency could even drops more with a more intense compression. More practical designs have been conducted with the available material properties in the lab. Measurements based on these practical designs present a similar tuning behavior as the simulation. Errors and losses that cause the mismatches between the measurements and simulations have been discussed. Some of them could be improved by a better manufacturing process. However this could not be improved too much due to the limitations on the 3-D printer.

Future Work

This work is able to demonstrate a static tuning mechanism. However, the mechanical tunable FSSs have a dramatic advantage of continues tuning. A more advanced prototype could be made in the future with a continuous compressible structure. A new design work is going to be considered due to the new prototype may need different materials. For example, we may use liquid metal as the conducing material, dielectric fluidics as the dielectric material and compressible foam for the substrate since all of them have the flexibility for continuous compression.

More work could also be done for controlling the two layers separately. The reconfiguration performance might also be changed due to different coordination between the two layers. Moreover, how the overlap of the disks between layers will affect the performance will also be interesting.

Another limitation in this design is the total number of unit cells used is too small. This is due to the plate element type itself is large and the S band waveguide has a fixed

dimension. In order to be able to be tested by the network analyzer, we could only keep a small number of unit cells to fit into the waveguide aperture. However, a larger array with more unit cells could be made and tested in a free-space measurement system (anechoic chamber with transmitting and receiving antennas) if possible in the future. Moreover, a better manufacturing method will be considered instead of using the 3-D printer in order to fabricate the model more efficiently and more accurately.

REFERENCES

[1] Benedikt A. Munk, "Frequency selective surfaces: theory and design," John Wiley and Sons, 2000.

[2] Mittra, R.; Chan, C.H.; Cwik, T., "Techniques for analyzing frequency selective surfaces-a review," *Proceedings of the IEEE*, vol.76, no.12, pp.1593, 1615, Dec. 1988.

[3] Abadi, M.S.H.; Shafai, C.; Shafai, L., "A reconfigurable frequency selective surface using switched slots in the ground plane," *Antenna Technology and Applied Electromagnetics & the American Electromagnetics Conference (ANTEM-AMEREM), 2010 14th International Symposium on* , vol., no., pp.1,4, 5-8 July 2010.

[4] Vardaxoglou, J.C., "Optical switching of frequency selective surface bandpass response," *Electronics Letters*, vol.32, no.25, pp.2345, 2346, 5 Dec 1996.

[5] Eric Kreit, Lydia M. Mäthger, Roger T. Hanlon, Patrick B. Dennis, Rajesh R. Naik, Eric Forsythe, Jason Heikenfeld , "Biological versus electronic adaptive coloration: how can one inform the other," DOI: 10.1098/rsif.2012.0601, Sep 2012.

[6] Huang, J.; Lee, S.W., "Tri-band frequency selective surface with circular ring elements," *Antennas and Propagation Society International Symposium*, 1991. AP-S. Digest, vol., no., pp.204, 207 vol.1, 24-28 June 1991.

[7] Vasylchenko, A.; Rottenberg, X.; Broze, B.X.; Nuytemans, M.; De Raedt, W.; Vandenbosch, G.A.E., "A frequency switchable antenna based on MEMS technology," *Antennas and Propagation (EuCAP), 2010 Proceedings of the Fourth European Conference on* , vol., no., pp.1,3, 12-16 April 2010.

[8] Sung, Y.J., "Reconfigurable Patch Antenna for Polarization Diversity," *Antennas and Propagation, IEEE Transactions on,* vol.56, no.9, pp.3053, 3054, Sept. 2008.

[9] S. Adhikari and K. Wu, "Developing one-dimensional electronically tunable microwave and millimeter-wave components and devices towards two-dimensional electromagnetically reconfigurable platform (invited paper)," *Progress in Electromagnetics Research,* Vol. 143, 821-848, 2013.

[10] Huff, G.H.; Rolando, D.L.; Walters, P.; McDonald, J., "A Frequency Reconfigurable Dielectric Resonator Antenna Using Colloidal Dispersions," *Antennas and Wireless Propagation Letters, IEEE,* vol.9, no., pp.288, 290, 2010.

[11] Huff, G.H.; Goldberger, S., "A Coaxial Stub Microfluidic Impedance Transformer (COSMIX)," *Microwave and Wireless Components Letters, IEEE* , vol.20, no.3, pp.154,156, March 2010.

[12] S. A. Long and G. H. Huff, "Experiments on a fluidic loading mechanism for beam-steering reflectarrays," in *Wireless Information Technology and Systems (ICWITS), 2010 IEEE International Conference on*, 2010, pp. 1-4.

[13] Barrera, J.D.; Huff, G.H., "Analysis of a Variable SIW Resonator Enabled by Dielectric Material Perturbations and Applications," *Microwave Theory and Techniques, IEEE Transactions on*, vol.61, no.1, pp.225, 233, Jan. 2013.

[14] Niroo-Jazi, M.; Denidni, T.A., "Reconfigurable dual-band frequency selective surfaces using a new hybrid element," *Antennas and Propagation (APSURSI), 2011 IEEE International Symposium on*, vol., no., pp.2673, 2676, 3-8 July 2011.

[15] Bossard, J.A.; Werner, D.H.; Mayer, T.S.; Drupp, Robert P., "A novel design methodology for reconfigurable frequency selective surfaces using genetic algorithms," *Antennas and Propagation, IEEE Transactions on* , vol.53, no.4, pp.1390,1400, April 2005.

[16] Zendejas, J.M.; Gianvittorio, J.P.; Rahmat-Samii, Y.; Judy, J.W., "Magnetic MEMS reconfigurable frequency-selective surfaces," *Microelectromechanical Systems, Journal of* , vol.15, no.3, pp.613,623, June 2006.

[17] Wenxun, Zhang; Hongxin, Song, "Analysis of mechanically tunable frequency selective surfaces," *Systems Engineering and Electronics, Journal of*, vol.8, no.4, pp.7, 16, Dec. 1997.

[18] I. Khodasevych, W. S. T. Rowe, and A. Mitchell, "Reconfigurable fishnet metamaterial using pneumatic actuation," *Progress In Electromagnetics Research B*, Vol. 38, 57-70, 2012.

[19] Azemi, S.N.; Ghorbani, K.; Rowe, W.S.T., "A Reconfigurable FSS Using a Spring Resonator Element," *Antennas and Wireless Propagation Letters, IEEE*, vol.12, no., pp.781, 784, 2013.

[20] David M. Pozar, “Microwave engineering, 4th edition” John Wiley and Sons, 2012.

[21] Getting Started with HFSS: Floquet Ports, Ansoft Corp., Pittsburgh, PA, 2007.

[22] Ahmadloo, M.; Mousavi, P., "A novel integrated dielectric-and-conductive ink 3D printing technique for fabrication of microwave devices," *Microwave Symposium Digest (IMS), 2013 IEEE MTT-S International* , vol., no., pp.1,3, 2-7 June 2013.

[23] Nakagawa, T.; Nakiri, T.; Hosoya, R.; Tajitsu, Y., "Electrical properties of biodegradable polylactic acid film," *IEEE Transactions on Industry Applications*, vol.40, no.4, pp.1020, 1024, July-Aug. 2004.